SIAM J. SCI. COMPUT.
Vol. 44, No. 6, pp. A3536–A3559

FAST L^2 OPTIMAL MASS TRANSPORT VIA REDUCED BASIS METHODS FOR THE MONGE–AMPÈRE EQUATION*

SHIJIN HOU†, YANLAI CHEN‡, AND YINHUA XIA†

Abstract. Repeatedly solving the parameterized optimal mass transport (pOMT) problem is a frequent task in applications such as image registration and adaptive grid generation. It is thus critical to develop a highly efficient reduced solver that is equally accurate as the full order model. In this paper, we propose such a machine learning–like method for pOMT by adapting a new reduced basis (RB) technique specifically designed for nonlinear equations, the reduced residual reduced over-collocation (R2-ROC) approach, to the parameterized Monge–Ampère equation. It builds on top of a narrow-stencil finite difference method (FDM), a so-called truth solver, which we propose in this paper for the Monge–Ampère equation with the transport boundary. Together with the R2-ROC approach, it allows us to handle the strong and unique nonlinearity pertaining to the Monge–Ampère equation achieving online efficiency without resorting to any direct approximation of the nonlinearity. Several challenging numerical tests demonstrate the accuracy and high efficiency of our reduced solver for solving the parameterized Monge–Ampère equation, effectively transporting the nontrivial boundaries.

Key words. parameterized optimal mass transport problem, Monge–Ampère equation, narrow-stencil finite difference method, transport boundary, reduced basis method, reduced residual reduced over-collocation approach

MSC codes. 65N06, 35J60, 65B99

DOI. 10.1137/21M1463720

1. Introduction.

The optimal mass transport (OMT) problem has received significant attention in recent years thanks to its wide applicability in areas such as image retrieval [48, 56], shape and image registration [37, 45], super-resolution reconstruction [43], cancer detection [4, 51], machine learning [32, 2, 21, 29, 44, 50], and adaptive grid generation [57], just to name a few. Among these applications, an interesting scenario emerges when the OMT problem needs to be solved repeatedly and often in a real-time manner. For example, in image processing, solving an OMT problem provides the optimal transformation between one pair of images out of potentially many that are closely related. Another example is that one OMT problem needs to be resolved for determining the grid movement in adaptive grid generation [57] for every round of a posteriori error estimation. Given appropriate parameterizations, these problems can be modeled by a parameterized optimal mass transport (pOMT) problem, the focus of the current paper.

Initially proposed by Monge [49] in the 18th century, OMT seeks the optimal

---

*Submitted to the journal's Methods and Algorithms for Scientific Computing section December 7, 2021; accepted for publication (in revised form) July 11, 2022; published electronically November 14, 2022.

https://doi.org/10.1137/21M1463720

Funding: The work of the second author was partially supported by National Science Foundation grant DMS-1719698, by a grant from the College of Arts & Sciences at the University of Massachusetts Dartmouth, and by the UMass Dartmouth Marine and UnderSea Technology (MUST) Research Program made possible via Office of Naval Research grant N00014-20-1-2849. The work of the third author was partially supported by National Natural Science Foundation of China grant 11871449.

†School of Mathematical Sciences, University of Science and Technology of China, Hefei, Anhui 230026, People's Republic of China (houshiji@mail.ustc.edu.cn, yhxia@ustc.edu.cn).

‡Department of Mathematics, University of Massachusetts Dartmouth, North Dartmouth, MA 02747 USA (yanlai.chen@umassd.edu).

mass-preserving transform between two distributions of mass for a given cost of transportation. Given two bounded and open domains $X, Y \in \mathbb{R}^d$, let $\nu_X(\boldsymbol{x}, \boldsymbol{\mu})$ be a probability measure on X, parameterized by a p-dimensional parameter $\boldsymbol{\mu} \in \mathcal{D} \subset \mathbb{R}^p$. $\nu_Y(\boldsymbol{y}, \boldsymbol{\mu}) = T_{\#}\nu_X$ is its push-forward on Y with a measurable map $T : X \mapsto Y$ satisfying the following mass-preserving property for any continuous function $h(\boldsymbol{y})$:

$$\int_Y h(\boldsymbol{y}) d\nu_Y(\boldsymbol{y}, \boldsymbol{\mu}) = \int_X h(T(\boldsymbol{x})) d\nu_X(\boldsymbol{x}, \boldsymbol{\mu}).$$

OMT seeks a minimizer of the cost functional $I(T) = \int_X c(\boldsymbol{x}, T(\boldsymbol{x})) d\nu_X(\boldsymbol{x}, \boldsymbol{\mu})$, where $c(\boldsymbol{x}, \boldsymbol{y})$ denotes the cost of transporting a unit of mass from the point $\boldsymbol{x} \in X$ to the point $\boldsymbol{y} \in Y$. If the measures are absolutely continuous with (parametric) positive densities $f_X(\boldsymbol{x}, \boldsymbol{\mu}), f_y(\boldsymbol{y}, \boldsymbol{\mu})$, that is,

$$d\nu_X(\boldsymbol{x}, \boldsymbol{\mu}) = f_X(\boldsymbol{x}, \boldsymbol{\mu}) d\boldsymbol{x}, \ d\nu_Y(\boldsymbol{y}, \boldsymbol{\mu}) = f_Y(\boldsymbol{y}, \boldsymbol{\mu}) d\boldsymbol{y},$$

by simple calculation, the mass balance condition could be rewritten as

$$\det\left(DT(\boldsymbol{x})\right) f_Y(T(\boldsymbol{x}), \boldsymbol{\mu}) = f_X(\boldsymbol{x}, \boldsymbol{\mu}), \tag{1.1}$$

where $\det\left(DT(\boldsymbol{x})\right)$ denotes the determinant of the Jacobian of $T(\boldsymbol{x})$. Although there are other formulations of this problem, such as Kantorovich formulation [41], we focus on the Monge formulation in this paper and aim to develop a fast solver for it. In the special case of the quadratic cost function $c(\boldsymbol{x}, \boldsymbol{y}) = \frac{1}{2}|\boldsymbol{x} - \boldsymbol{y}|^2$, the minimizing map $T(\boldsymbol{x})$ can be expressed as the gradient of a convex function [22, 54] justifying a substitution of T by ∇u in (1.1). This results in the following parametric Monge–Ampère equation, which is augmented by the convexity constraint on u for uniqueness and stability [1, 34]. We also enforce the so-called transport or second boundary condition (1.2b):

$$\det\left(D^2 u(\boldsymbol{x}, \boldsymbol{\mu})\right) = \frac{f_X(\boldsymbol{x}, \boldsymbol{\mu})}{f_Y(\nabla u(\boldsymbol{x}, \boldsymbol{\mu}), \boldsymbol{\mu})}, \ \boldsymbol{x} \in X, \tag{1.2a}$$

$$\nabla u(X, \boldsymbol{\mu}) = Y, \tag{1.2b}$$

$$u(\boldsymbol{x}, \boldsymbol{\mu}) \text{ is convex in X.} \tag{1.2c}$$

Here, $D^2 u(x)$ denotes the Hessian of the function u. The challenge in solving (1.2) resides in the strong nonlinearity, the convexity constraint, the difficulty of approximating the transport boundary condition, and the low regularity of its solution. The literature on numerical methods is therefore rather scarce. Benamou and Brenier [5] presented a fluid flow approach which was further developed by Haber, Rehman, and Tannenbaum [36]. The method is computationally expensive due to the introduction of an additional dimension. More recently, Froese [27] proposed an approach for solving (1.2) by iteratively solving a sequence of Neumann boundary value problems of the Monge–Ampère equation and proved that the numerical solution converges to the viscosity solution. Benamou, Froese, and Oberman [6] developed an approach by reformulating the transport boundary condition by an implicit Hamilton–Jacobi equation and gave the proof of convergence.

The situation is exacerbated by the need to solve the problem for a large number of parameter values. To the best of our knowledge, there is no existing work based on systematic model order reduction for the parameterized Monge–Ampère equation. In this article, we aim to provide the *first such work*. Our first contribution is the proposal of a truth solver by extending the narrow-stencil finite difference scheme of [23], originally designed for the Hamilton–Jacobi–Bellman equations, to our context. An improvement of the standard finite difference scheme, this narrow-stencil scheme is amenable to the reduced basis (RB) framework while being more robust in handling singular solutions thanks to the introduction of the artificial viscosity and numerical moment. In addition, we adopt the framework of [27] in dealing with the transport boundary. The reduced residual reduced over-collocation (R2-ROC) method proposed in [14] serves as our reduced order modeling approach. The R2-ROC is a class of reduced basis methods (RBMs) [53, 38, 35] specifically designed for nonlinear and nonaffine problems. Like RBM, but based on an underlying scheme of a nodal form, it features an offline/online decomposition strategy, the a posteriori error estimator/indicator, and a classical greedy algorithm. The main task of the offline phase is to construct a problem-dependent, low-dimensional surrogate space and set the stage for online computations. After the (time-consuming) offline stage, the full speed of the method will then be appreciated online when the reduced solver is performed on demand and usually with a cost only dependent on the (much lower) RB space dimension. Due to the strong nonlinearity of the Monge–Ampère equation, the classical RBM will suffer on its online complexity resulting from its dependence on the number of (discrete) empirical interpolation method (EIM/DEIM) [3, 12, 33] terms. The R2-ROC method eliminates this dependence by augmenting and extending the EIM approach as a direct PDE solver, judiciously determining a set of over-collocation points, and taking advantage of the simplicity of evaluating the hyper-reduced well-chosen residuals. It achieves offline/online computation efficiency and, more interestingly, the independence of the number of EIM/DEIM expansion terms. Our second contribution of this paper is to adapt the R2-ROC method, designed for the classical Dirichlet or Neumann boundary conditions, for the much more intricate transport boundary condition imposed by the Monge–Ampère equation.

The organization of this paper is as follows. In section 2, we review some theoretical results for the Monge–Ampère equation before describing an iterative algorithm for implementing the transport boundary condition and a narrow-stencil finite difference scheme for approximating the Monge–Ampère equation. The combination of them provides an efficient full order model (FOM). In section 3, we introduce the R2-ROC method and our adaptation to the transport boundary case toward our reduced order model. In section 4, we present numerical results for the Monge–Ampère equation and the parameterized Monge–Ampère equation to demonstrate the efficiency and accuracy of our methods. Concluding remarks are made in section 5.

2. A narrow-stencil finite difference method for L^2 optimal mass transport problem.

This section is devoted to a detailed description of our truth solver, an extension of the narrow-stencil finite difference scheme of [23] to the Monge–Ampère equation adopting the framework of [27] in dealing with the transport boundary condition. In order to properly inform the numerical scheme, it is important to know when a classical C^2 solution exists. Toward that end, we first review some regularity results for the Monge–Ampère equation.

2.1. Regularity.

The classical C^2 solution of the Monge–Ampère-type equation exists under certain regularity conditions on the data and computational domains. We present below the regularity results for the Dirichlet boundary value problem

$$\det(D^2u(\boldsymbol{x})) = f(\boldsymbol{x}),\ \boldsymbol{x} \in X, \tag{2.1a}$$

$$u(\boldsymbol{x}) = g(\boldsymbol{x}),\ \boldsymbol{x} \in \partial X, \tag{2.1b}$$

and then the transport boundary value problem (1.2).

Theorem 2.1 (see [60, 7]). *Suppose that X is strictly convex with boundary $\partial X \in C^{2,\alpha}$.*[1] *Suppose also that the function $f \in C^{\alpha}(X)$ is strictly positive and the boundary values $g \in C^{2,\alpha}(\partial X)$. Then the Dirichlet boundary value problem of Monge–Ampère equation (2.1) has a unique $C^{2,\alpha}$ solution.*

Theorem 2.2 (interior regularity [8, 9]). *Suppose that X, Y are bounded, connected, open sets and Y is convex. Suppose also that the density functions*

$$f_X : X \to (0,\infty),\ f_Y : Y \to (0,\infty)$$

are bounded away from 0 and ∞. Then the solution of the Monge–Ampère equation (1.2) belongs to $C^{1,\alpha}(X)$ for some $0<\alpha<1$. If , in addition, the density function $f, g \in C^{\beta}$ for some $0<\beta<1$, then the solution of the Monge–Ampère equation belongs to $C^{2,\alpha}$ for every $0<\alpha<\beta$.

2.2. Transport boundary condition. In this section, we describe an efficient algorithm proposed in [27] for dealing with the transport condition (1.2b). Indeed, when X, Y are both convex, the transport condition can be enforced by requiring that the boundary points of X are mapped to the boundary points of Y [52, 58, 59]. That is,

$$\nabla u(\boldsymbol{\mu}) : \partial X \mapsto \partial Y.$$

Assuming that the boundary of the target region ∂Y can be represented as the zeroth level set of a function Φ, we have that the transport map must satisfy

$$\Phi(\nabla u(\boldsymbol{x};\boldsymbol{\mu})) = 0,\ \boldsymbol{x} \in \partial X. \tag{2.2}$$

The appearance of the gradient and the simplicity of implementing a Neumann boundary condition motivated the authors of [27] to replace the condition (2.2) with the Neumann boundary condition

$$\nabla u(\boldsymbol{x};\boldsymbol{\mu}) \cdot \boldsymbol{n}(\boldsymbol{x}) = \phi(\boldsymbol{x};\boldsymbol{\mu}),$$

where $\phi(\boldsymbol{x};\boldsymbol{\mu})$ is a function to be determined and $\boldsymbol{n}$ denotes the unit outward normal. Froese [27] further proposed the following iterative approach for approximating the function $\phi(\boldsymbol{x};\boldsymbol{\mu})$. Given the kth iteration $u^k(\boldsymbol{x};\boldsymbol{\mu})$ of the approximate solution to the Monge–Ampère equation with the transport boundary condition, we proceed to the next iteration as follows. We first compute $\phi^k(\boldsymbol{x};\boldsymbol{\mu})$ for $\boldsymbol{x} \in \partial X$ via

$$\phi^k(\boldsymbol{x};\boldsymbol{\mu}) = \mathbb{P}_{\partial Y}(\nabla u^k(\boldsymbol{x};\boldsymbol{\mu})) \cdot \boldsymbol{n}(\boldsymbol{x}), \tag{2.3}$$

where $\mathbb{P}_{\partial Y}(\boldsymbol{v})$ denotes the shortest-distance projection of $\boldsymbol{v}$ onto the set ∂Y: $\mathbb{P}_{\partial Y}(\boldsymbol{v}) = \arg\min_{\boldsymbol{w}\in\partial Y} ||\boldsymbol{w}-\boldsymbol{v}||^2_{L^2}$.

After that, we find a convex function $u^{k+1}(\boldsymbol{x};\boldsymbol{\mu}) : X \mapsto \mathbb{R}$ and a constant $\sigma^{k+1}(\boldsymbol{\mu}) \in R^+$ such that

$$\det(D^2 u^{k+1}(\boldsymbol{x};\boldsymbol{\mu})) = \sigma^{k+1}(\boldsymbol{\mu}) \frac{f_X(\boldsymbol{x};\boldsymbol{\mu})}{\widehat{f_Y}(\nabla u^{k+1}(\boldsymbol{x};\boldsymbol{\mu});\boldsymbol{\mu})},\ \boldsymbol{x} \in X, \tag{2.4a}$$

$$\int_X u^{k+1}(\boldsymbol{x};\boldsymbol{\mu}) dx = 0, \tag{2.4b}$$

$$\nabla u^{k+1}(\boldsymbol{x};\boldsymbol{\mu}) \cdot \boldsymbol{n}(\boldsymbol{x}) = \phi^k(\boldsymbol{x};\boldsymbol{\mu}),\ \boldsymbol{x} \in \partial X. \tag{2.4c}$$

---

[1] The Hölder space $C^{k,\alpha}(\Omega)$, where Ω is an open subset of some Euclidean space and $k \geq 0$ an integer, consists of those functions on Ω having continuous derivatives up through order k and such that the kth partial derivatives are Hölder continuous with exponent α, where $0 < \alpha \leq 1$ [30].

Here, $\widehat{f_Y}(\boldsymbol{y};\boldsymbol{\mu})$ is the extended target density function of $f_Y(\boldsymbol{y};\boldsymbol{\mu})$ defined as

$$\widehat{f_Y}(\boldsymbol{y};\boldsymbol{\mu}) = \begin{cases} f_Y(\boldsymbol{y};\boldsymbol{\mu}), \ \boldsymbol{y} \in Y, \\ f_Y(\boldsymbol{y}_0;\boldsymbol{\mu}), \ \boldsymbol{y} \notin Y, \end{cases}$$

where $\boldsymbol{y}_0$ is a point in the interior of the target set Y. This extension assigns positive values outside of Y to accommodate the fact that it is a density and, during iterations, ∇u^{k+1} in (2.4a) may map (part of) X out of Y. It is worth noting that more complex extensions with higher regularity may be required for the convergence of the Monge–Ampère solver; see [27]. We adopt this simple position extension of $f_Y(\boldsymbol{y};\boldsymbol{\mu})$, which is enough for our solver introduced in section 2.3. This iteration proceeds until the difference between u^k and u^{k+1} is sufficiently small. To start it, we simply let $\phi^{-1}(\boldsymbol{x};\boldsymbol{\mu}) = B\boldsymbol{x}\cdot\boldsymbol{n}(\boldsymbol{x})$, where $B > 0$ is large enough to ensure the set $\{B\boldsymbol{x} \mid \boldsymbol{x} \in X\}$ contains Y.

Remark 2.3. As is well known, the solution of the Neumann boundary value problems may not exist. Even if it exists, the solution is unique only up to a constant. For these reasons, the variable $\sigma^{k+1}(\boldsymbol{\mu})$ in (2.4a) and the mean-zero condition (2.4b) are introduced. The projection $\mathbb{P}_{\partial Y}(\boldsymbol{v})$ is introduced to mitigate the misalignment of $\nabla u^k(\partial X;\boldsymbol{\mu})$ and ∂Y, which contributes to obtaining the correct choice of $\phi(\boldsymbol{x};\boldsymbol{\mu})$.

Remark 2.4. An L^2 optimal mapping does not lead to twisting or rotation. When we consider the simple case of mapping a rectangle to another rectangle, each side of X will be mapped to the corresponding side of Y. Since the directional derivative of u at $\boldsymbol{x} \in \partial X$ is determined, we obtain an exact Neumann boundary condition. In this case, the transport boundary problem becomes a Neumann boundary value problem.

2.3. Discretization for the Monge–Ampère equation.

With the iterative framework for the transport problem, we propose to incorporate a finite difference solver [47, 23] for the Neumann boundary value problems (2.4) which would conclude the description of our FOM. This finite difference solver adopts artificial viscosity and moment terms to regularize a standard finite difference scheme. To describe it in detail, we first fix some notations. Assume that X is a d-dimensional hypercube, i.e., $X = \prod_{i=1}^d (a_i, b_i)$. We distribute $\mathcal{N}_i$ grid points uniformly on the ith dimension and define

$$h_i = \frac{b_i - a_i}{\mathcal{N}_i - 1}, \ \mathcal{N} = \prod_{i=1}^d \mathcal{N}_i, \ \text{and } \Theta = \left\{\theta = (\theta_1, \theta_2, \ldots, \theta_d) \middle| 1 \le \theta_i \le \mathcal{N}_i, i = 1, 2, \ldots, d\right\}.$$

Then we denote the rectangular mesh by $\mathcal{T}_h = \{\prod_{i=1}^d (a_i + (\theta_i - 1)h_i, a_i + \theta_i h_i) | \theta \in \Theta\}$ and the grid points set by $X^{\mathcal{N}} = \{\boldsymbol{x}_\theta = (a_1 + (\theta_1 - 1)h_1, a_2 + (\theta_2 - 1)h_2, \ldots, a_d + (\theta_d - 1)h_d) | \theta \in \Theta\}$. The finite difference approximation of $u(\boldsymbol{x};\boldsymbol{\mu})$ on the grid $\mathcal{T}_h$ is denoted by $u^{\mathcal{N}}(\boldsymbol{x}_\theta;\boldsymbol{\mu})$. With appropriate rearrangement, the approximation $u^{\mathcal{N}}(\boldsymbol{\mu}) = u^{\mathcal{N}}(X^{\mathcal{N}};\boldsymbol{\mu})$ can be regarded as an $\mathcal{N} \times 1$ vector and represent our numerical solution.

2.3.1. Difference operators.

We first introduce several difference operators for approximating the first and second derivatives. Let $\delta_{x_i}^{\pm} u^{\mathcal{N}}(\boldsymbol{x}_\theta;\boldsymbol{\mu})$ denote the standard forward and backward finite difference operators. That is,

$$\delta_{x_i}^{+} u^{\mathcal{N}}(\boldsymbol{x}_\theta;\boldsymbol{\mu}) := \frac{u^{\mathcal{N}}(\boldsymbol{x}_\theta + h_i\boldsymbol{e}_i;\boldsymbol{\mu}) - u^{\mathcal{N}}(\boldsymbol{x}_\theta;\boldsymbol{\mu})}{h_i},$$
$$\delta_{x_i}^{-} u^{\mathcal{N}}(\boldsymbol{x}_\theta;\boldsymbol{\mu}) := \frac{u^{\mathcal{N}}(\boldsymbol{x}_\theta;\boldsymbol{\mu}) - u^{\mathcal{N}}(\boldsymbol{x}_\theta - h_i\boldsymbol{e}_i;\boldsymbol{\mu})}{h_i},$$

where $\{\boldsymbol{e}_i\}_{i=1}^d$ denote the canonical basis vectors for $\mathbb{R}^d$. The central difference operator is $\delta_{x_i} := \frac{1}{2}(\delta_{x_i}^+ + \delta_{x_i}^-)$. Naturally, we can define the gradient operators ∇_h^+, ∇_h^-, and ∇_h by

$$\nabla_h^{\pm} := [\delta_{x_1}^{\pm}, \delta_{x_2}^{\pm}, \ldots, \delta_{x_d}^{\pm}]^T,\ \nabla_h := [\delta_{x_1}, \delta_{x_2}, \ldots, \delta_{x_d}]^T.$$

Various compositions of these operators will approximate the second derivatives $\partial_{x_i x_j}^2$. Indeed, for $\mu, \nu \in \{+,-\}$, $D_{h,ij}^{\mu\nu} := \delta_{x_j}^{\nu} \delta_{x_i}^{\mu}$ are approximations of $\partial_{x_i x_j}^2$. They naturally induce the approximations of the Hessian operator

$$D_h^{\mu\nu} := [D_{h,ij}^{\mu\nu}]_{i,j=1}^d,\ \mu, \nu \in \{+,-\}.$$

For our purpose, we will adopt the following two second order accurate approximations:

$$\overline{D}_h^2 := \frac{D_h^{+-} + D_h^{-+}}{2},\ \widetilde{D}_h^2 := \frac{D_h^{++} + D_h^{--}}{2}.$$

2.3.2. The narrow-stencil finite difference scheme.

We are now ready to describe the narrow-stencil finite difference scheme for the Monge–Ampère equation. We start by rewriting the Monge–Ampère operator in (2.4a) in the following form:

$$G(D^2u(\boldsymbol{x};\boldsymbol{\mu}), \nabla u(\boldsymbol{x};\boldsymbol{\mu}), u(\boldsymbol{x};\boldsymbol{\mu}), \boldsymbol{x}, \sigma(\boldsymbol{\mu})) := \sigma(\boldsymbol{\mu}) \frac{f_X(\boldsymbol{x};\boldsymbol{\mu})}{\widehat{f_Y}(\nabla u(\boldsymbol{x};\boldsymbol{\mu});\boldsymbol{\mu})} - \det(D^2 u(\boldsymbol{x};\boldsymbol{\mu})).$$

Then the narrow-stencil finite difference scheme seeks a grid function $u^{\mathcal{N}}(\boldsymbol{x}_\theta;\boldsymbol{\mu})$ for all $\boldsymbol{x}_\theta \in X^{\mathcal{N}}$ such that $\widehat{G}(u^{\mathcal{N}}(\boldsymbol{x}_\theta;\boldsymbol{\mu}), \boldsymbol{x}_\theta, \sigma(\boldsymbol{\mu})) = 0$, where the numerical Monge–Ampère operator is defined as

(2.5)
$$\begin{aligned} \widehat{G}(u^{\mathcal{N}}(\boldsymbol{x}_\theta;\boldsymbol{\mu}), \boldsymbol{x}_\theta, \sigma(\boldsymbol{\mu})) &= G(\overline{D}_h^2 u^{\mathcal{N}}(\boldsymbol{x}_\theta;\boldsymbol{\mu}), \nabla_h u^{\mathcal{N}}(\boldsymbol{x}_\theta;\boldsymbol{\mu}), u^{\mathcal{N}}(\boldsymbol{x}_\theta;\boldsymbol{\mu}), \boldsymbol{x}_\theta, \sigma(\boldsymbol{\mu})) \\ &\quad + 2A : (\widetilde{D}_h^2 u^{\mathcal{N}}(\boldsymbol{x}_\theta;\boldsymbol{\mu}) - \overline{D}_h^2 u^{\mathcal{N}}(\boldsymbol{x}_\theta;\boldsymbol{\mu})) - \boldsymbol{b} \cdot (\nabla_h^+ u^{\mathcal{N}}(\boldsymbol{x}_\theta;\boldsymbol{\mu}) - \nabla_h^- u^{\mathcal{N}}(\boldsymbol{x}_\theta;\boldsymbol{\mu})). \end{aligned}$$

In this equation, $A(u^{\mathcal{N}}(\boldsymbol{x}_\theta;\boldsymbol{\mu}), \boldsymbol{x}_\theta) : \mathbb{R}^{\mathcal{N}} \times X^{\mathcal{N}} \to \mathbb{R}^{d\times d}$ is a matrix-valued function and $\boldsymbol{b}(u^{\mathcal{N}}(\boldsymbol{x}_\theta;\boldsymbol{\mu}), \boldsymbol{x}_\theta) : \mathbb{R}^{\mathcal{N}} \times X^{\mathcal{N}} \to \mathbb{R}^d$ is vector-valued. In this article, we simply choose $A = \alpha I$ and $\boldsymbol{b} = \beta \boldsymbol{e}$ for $\alpha \geq 0$ and $\beta \geq 0$, where I denotes the $d \times d$ identity matrix and $\boldsymbol{e}$ the d-dimensional column vector with all elements equal to 1.

Next, we introduce the discretization of the uniqueness and boundary conditions (2.4b) and (2.4c). Since (2.5) is an approximation of the fourth order PDE, we have to introduce an additional boundary condition to guarantee that the discrete problem is well-posed. As [25] has done, here we introduce one discrete additional boundary condition

$$\nabla_h(\Delta_h u^{\mathcal{N}}(\boldsymbol{x}_\theta;\boldsymbol{\mu})) \cdot \boldsymbol{n}(\boldsymbol{x}_\theta) = 0,\ \boldsymbol{x}_\theta \in X^{\mathcal{N}} \cap \partial X, \tag{2.6}$$

where discrete operator Δ_h is defined by the nine-point finite difference scheme. For the transport boundary condition (2.2), we simply discretize the gradient by the central difference

$$\Phi(\nabla_h u^{\mathcal{N}}(\boldsymbol{x}_\theta;\boldsymbol{\mu})) = 0,\ \boldsymbol{x}_\theta \in X^{\mathcal{N}} \cap \partial X. \tag{2.7}$$

We finish by discretizing the uniqueness condition via the mean value of each component of vector $u^{\mathcal{N}}(\boldsymbol{\mu})$,

$$\frac{\sum_{\boldsymbol{x}_\theta \in X^{\mathcal{N}}} u^{\mathcal{N}}(\boldsymbol{x}_\theta;\boldsymbol{\mu})}{\mathcal{N}} = 0. \tag{2.8}$$

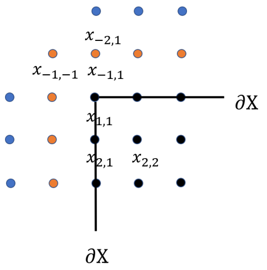

FIG. 1. *Schematic of the ghost points.*

This system can be solved by Newton's method efficiently, with details on initialization provided in section 2.4. We note here that handling the boundary conditions (2.6), (2.7) will require the introduction of two layers of ghost points as depicted in Figure 1. The values at the first layer of ghost points near the boundary are determined by the boundary condition. For instance, the normal derivative in the direction $\boldsymbol{n}_{x_1}$ at point $\boldsymbol{x}_{1,1}$ can be discretized as

$$u_{\boldsymbol{n}_{x_1}}(\boldsymbol{x}_{1,1};\boldsymbol{\mu}) \approx \frac{1}{2h_1}(u^{\mathcal{N}}(\boldsymbol{x}_{-1,1};\boldsymbol{\mu}) - u^{\mathcal{N}}(\boldsymbol{x}_{2,1};\boldsymbol{\mu})).$$

In the general case, we define the normal derivative in the diagonal direction at the four corners by the sum of the normal derivative in two orthogonal outward directions and still apply the central difference scheme to discretize the derivative:

$$\begin{aligned} u_{\boldsymbol{n}_{\text{diag}}}(\boldsymbol{x}_{1,1};\boldsymbol{\mu}) &\approx \frac{1}{2\sqrt{h_1^2+h_2^2}}(u^{\mathcal{N}}(\boldsymbol{x}_{-1,-1};\boldsymbol{\mu}) - u^{\mathcal{N}}(\boldsymbol{x}_{2,2};\boldsymbol{\mu}))\\ &= \frac{1}{\sqrt{2}}(u_{\boldsymbol{n}_{x_1}}(\boldsymbol{x}_{1,1};\boldsymbol{\mu}) + u_{\boldsymbol{n}_{x_2}}(\boldsymbol{x}_{1,1};\boldsymbol{\mu})). \end{aligned}$$

The values of the most outer ghost points are determined by the additional boundary condition (2.6), for example

$$\begin{aligned} 0 &= \frac{\partial \Delta_h u^{\mathcal{N}}(\boldsymbol{x}_{1,1};\boldsymbol{\mu})}{\partial \boldsymbol{n}_{x_1}}\\ &= \frac{\left(\frac{u^{\mathcal{N}}(\boldsymbol{x}_{-2,1};\boldsymbol{\mu}) - 2u^{\mathcal{N}}(\boldsymbol{x}_{-1,1};\boldsymbol{\mu}) + u^{\mathcal{N}}(\boldsymbol{x}_{1,1};\boldsymbol{\mu})}{h_1^2} + \delta_{x_2}^2 u^{\mathcal{N}}(\boldsymbol{x}_{-1,1};\boldsymbol{\mu})\right) - (\delta_{x_1}^2 + \delta_{x_2}^2)u^{\mathcal{N}}(\boldsymbol{x}_{2,1};\boldsymbol{\mu})}{2h_1}, \end{aligned}$$

which means that

$$u^{\mathcal{N}}(\boldsymbol{x}_{-2,1};\boldsymbol{\mu}) = -u^{\mathcal{N}}(\boldsymbol{x}_{1,1};\boldsymbol{\mu}) + 2u^{\mathcal{N}}(\boldsymbol{x}_{-1,1};\boldsymbol{\mu}) + h_1^2(-\delta_{x_2}^2 u^{\mathcal{N}}(\boldsymbol{x}_{-1,1};\boldsymbol{\mu}) + (\delta_{x_1}^2 + \delta_{x_2}^2)u^{\mathcal{N}}(\boldsymbol{x}_{2,1};\boldsymbol{\mu})).$$

Remark 2.5. This scheme only entails a 14-point stencil in two dimensions. By contrast, the monotone finite difference method (FDM) of [28] needs more points because of the discrete-direction error. For this reason, it is called the narrow-stencil scheme. We next examine the last two terms in the scheme (2.5) to reveal that the narrow-stencil FDM introduces the stabilization terms, i.e., numerical moment and numerical viscosity [24, 26, 20]. Indeed, a direct calculation shows that

$$\begin{aligned} (\delta_{x_i}^+ - \delta_{x_i}^-)u^{\mathcal{N}}(\boldsymbol{x}_\theta;\boldsymbol{\mu}) &= h_i \frac{u^{\mathcal{N}}(\boldsymbol{x}_\theta - h_i\boldsymbol{e}_i;\boldsymbol{\mu}) - 2u^{\mathcal{N}}(\boldsymbol{x}_\theta;\boldsymbol{\mu}) + u^{\mathcal{N}}(\boldsymbol{x}_\theta + h_i\boldsymbol{e}_i;\boldsymbol{\mu})}{h_i^2}\\ &= h_i \delta_{x_i}^2 u^{\mathcal{N}}(\boldsymbol{x}_\theta;\boldsymbol{\mu}). \end{aligned}$$

Therefore, $\beta \boldsymbol{e}\cdot(\nabla_h^+ - \nabla_h^-)u^{\mathcal{N}}(\boldsymbol{x}_\theta;\boldsymbol{\mu}) \approx \beta h \Delta u(\boldsymbol{x}_\theta;\boldsymbol{\mu})$, which amounts to addition of numerical viscosity, a known technique for constructing a convergent difference scheme; see, e.g., [20]. Further, we can show that, for all $i, j \in \{1, 2, \dots, d\}$,

$$\begin{aligned}(\widetilde{D}^2_{h,ij} - \overline{D}^2_{h,ij})u^{\mathcal{N}}(\boldsymbol{x}_\theta;\boldsymbol{\mu}) &= \frac{1}{2}(\delta^+_{x_i}\delta^+_{x_j} + \delta^-_{x_i}\delta^-_{x_j} - \delta^+_{x_i}\delta^-_{x_j} - \delta^-_{x_i}\delta^+_{x_j})u^{\mathcal{N}}(\boldsymbol{x}_\theta;\boldsymbol{\mu})\\ &= \frac{h_i h_j}{2}\delta^2_{x_i}\delta^2_{x_j}u^{\mathcal{N}}(\boldsymbol{x}_\theta;\boldsymbol{\mu}).\end{aligned}$$

This means that

$$\alpha I : (\widetilde{D}^2_h - \overline{D}^2_h)u^{\mathcal{N}}(\boldsymbol{x}_\theta;\boldsymbol{\mu}) \approx \alpha h^2 \Delta^2 u(\boldsymbol{x}_\theta;\boldsymbol{\mu}),$$

which introduces the numerical moment in the vanishing moment method of [24]. Synthesizing the above observations, it is clear that the proposed scheme is an approximation of the following fourth order quasilinear PDE:

$$\alpha h^2 \Delta^2 u(\boldsymbol{x};\boldsymbol{\mu}) - \beta h \Delta u(\boldsymbol{x};\boldsymbol{\mu}) + G(D^2 u(\boldsymbol{x};\boldsymbol{\mu}), \nabla u(\boldsymbol{x};\boldsymbol{\mu}), u(\boldsymbol{x};\boldsymbol{\mu}), \boldsymbol{x}, \sigma(\boldsymbol{\mu})) = 0,$$

which is a regularization of the original nonlinear PDE.

2.4. The algorithm for the transport boundary problem. Integrating the iterative approach for the transport boundary condition with the narrow-stencil finite difference scheme for the Neumann boundary value subproblem, we are ready to present our FOM for the transport boundary problem of the Monge–Ampère equation. Indeed, due to the (exact) transport boundary condition (2.2) being turned into the sequence of Neumann boundary conditions (2.4c), the discretized transport boundary condition (2.7) is also replaced by a sequence of discretized Neumann boundary conditions of the type

$$\nabla_h u^{\mathcal{N},k+1}(\boldsymbol{x}_\theta;\boldsymbol{\mu}) \cdot \boldsymbol{n}(\boldsymbol{x}_\theta) = \phi^k(\boldsymbol{x}_\theta),\ \boldsymbol{x}_\theta \in X^{\mathcal{N}} \cap \partial X. \tag{2.9}$$

Hence, for a given ϕ^k, we define the nonlinear problem as solving for $(u^{\mathcal{N},k+1}, \sigma^{k+1})^T$ such that they satisfy (2.5) with the boundary condition (2.6) and the uniqueness condition (2.8), all with $(u^{\mathcal{N}}, \sigma)^T$ replaced by $(u^{\mathcal{N},k+1}, \sigma^{k+1})^T$ and the Neumann boundary condtion (2.9). For notational simplicity, we denote the whole system of equations encompassing (2.5), (2.6), (2.8), and (2.9) by

$$F(u^{\mathcal{N},k+1}(\boldsymbol{\mu}), \sigma^{k+1}(\boldsymbol{\mu}); \phi^k(X^{\mathcal{N}} \cap \partial X;\boldsymbol{\mu})) = 0. \tag{2.10}$$

We are now ready to present the algorithm for solving the problem (1.2) for a given value of $\boldsymbol{\mu}$, in Algorithm 2.1, with the Neumann boundary data $\phi^k(X^{\mathcal{N}} \cap \partial X;\boldsymbol{\mu})$ being given an initial value and then corrected, after every solve of (2.10), through projecting the mapping $\nabla_h u^{\mathcal{N},k+1}(\boldsymbol{\mu})(X^{\mathcal{N}} \cap \partial X;\boldsymbol{\mu})$ to ∂Y. Newton's method is used for rapidly solving the nonlinear system (2.10). To assist with the convergence of Newton's method, an initialization sufficiently close to the exact solution is necessary. We adopt the approach of [28] and take the initial value of the kth iteration, $(u_0^{\mathcal{N},k}(X^{\mathcal{N}};\boldsymbol{\mu}), \sigma_0^k(\boldsymbol{\mu}))^T$, as the solution of

$$\begin{aligned}&\Delta_h u^{\mathcal{N}}(\boldsymbol{x}_\theta;\boldsymbol{\mu}) = \sigma(\boldsymbol{\mu})\left(\frac{2 f_X(\boldsymbol{x}_\theta;\boldsymbol{\mu})}{f_Y(\boldsymbol{x}_\theta - \boldsymbol{y}_0;\boldsymbol{\mu})}\right)^{\frac{1}{2}},\ \boldsymbol{x}_\theta \in X^{\mathcal{N}},\\ &\frac{\sum_{\boldsymbol{x}_\theta \in X^{\mathcal{N}}} u^{\mathcal{N}}(\boldsymbol{x}_\theta;\boldsymbol{\mu})}{\mathcal{N}} = 0,\\ &\nabla_h u^{\mathcal{N}}(\boldsymbol{x}_\theta;\boldsymbol{\mu}) \cdot \boldsymbol{n}(\boldsymbol{x}_\theta) = \phi^k(\boldsymbol{x}_\theta),\ \boldsymbol{x}_\theta \in X^{\mathcal{N}} \cap \partial X.\end{aligned}$$

Algorithm 2.1 The algorithm for the transport boundary problem of Monge–Ampère equation

```
Set $\phi^{-1}(\boldsymbol{x};\boldsymbol{\mu}) = B\boldsymbol{x}\cdot\boldsymbol{n}$ for sufficient large $B$, the error tolerance $\epsilon$, and the maximum number of iterations $K$. Compute $(u^{\mathcal{N},0}(\boldsymbol{\mu}),\sigma^0(\boldsymbol{\mu}))^T$ by solving $F(u^{\mathcal{N}}(\boldsymbol{\mu}),\sigma(\boldsymbol{\mu});\phi^{-1}(X^{\mathcal{N}}\cap\partial X;\boldsymbol{\mu}))=0$.
Initialize $k=0$ and $r=1$.
while $r\geq\epsilon$ and $k<K$ do
    Compute $\phi^k(\boldsymbol{x}_\theta;\boldsymbol{\mu}) = \mathbb{P}_{\partial Y}(\nabla_h u^{\mathcal{N},k}(\boldsymbol{x}_\theta;\boldsymbol{\mu}))\cdot\boldsymbol{n}$ for $\boldsymbol{x}_\theta\in X^{\mathcal{N}}\cap\partial X$.
    Compute $(u^{\mathcal{N},k+1}(\boldsymbol{\mu}),\sigma^{k+1}(\boldsymbol{\mu}))^T$ by solving $F(u^{\mathcal{N}}(\boldsymbol{\mu}),\sigma(\boldsymbol{\mu});\phi^k(X^{\mathcal{N}}\cap\partial X;\boldsymbol{\mu}))=0$.
    Compute the relative error $r=||u^{\mathcal{N},k+1}(\boldsymbol{\mu})-u^{\mathcal{N},k}(\boldsymbol{\mu})||_{\ell^\infty(\mathbb{R}^{\mathcal{N}})}$.
    Let $k=k+1$.
end while
```

3. The reduced residual reduced over-collocation (R2-ROC) method. Following the FOM presented in the last section, we introduce our proposed reduced order model (ROM) for the transport boundary problem of the Monge–Ampère equation. Specifically, we adopt the reduced over-collocation (ROC) approach [14] developed for parameterized nonlinear partial differential equations. The unique feature is the immunity to the degradation in online efficiency suffered by classical RBM due to the EIM-like expansion of the nonlinear and nonaffine terms. To illustrate the algorithm, we first recall that we denote by $u(\boldsymbol{x};\boldsymbol{\mu})$ the exact solution of the Monge–Ampère equation (1.2), which is nonlinear and parameterized in a nonaffine fashion by $\boldsymbol{\mu}$. Moreover, the resulting FOM solution corresponding to parameter $\boldsymbol{\mu}$ is denoted by $u^{\mathcal{N}}(X^{\mathcal{N}};\boldsymbol{\mu})$, which we assume is close enough to the exact solution $u(\boldsymbol{x};\boldsymbol{\mu})$ for us to adopt as a reference for the ROM. Now we are ready to briefly review the R2-ROC algorithm. We first note that it is an RBM exploiting the full advantages of nodal form solvers both offline and online. It can be viewed as adopting hyper-reduction for reduced residual minimization. Hyper-reduction approaches include the EIM [3], the DEIM [12], Gauss–Newton approximation tensor (GNAT) [10] and its extensions [18, 19], nonlinear manifold least-squares Petrov–Galerkin (NM-LSPG) [46] utilizing GNAT, and autoencoders [31]. R2-ROC, instead of reconstructing the residuals on a global basis like GNAT, which can be inefficient, collocates them on some well-chosen nodes. The method was integrated with NM-LSPG and convolutional autoencoders for some nonlinear manifold hyper-reduced ROMs [55] achieving accuracy and interpretability. R2-ROC has two components: an online (reduced) solver of size n that is between 1 and N with N usually much smaller than $\mathcal{N}$, and an offline training component which repeatedly calls the online solver of increasing size n to build up a surrogate solution space from scratch dimension-by-dimension.

Online solver. Given the reduced space W_n and a collocation set X^m, a subset of the full grid $X^{\mathcal{N}}$, of cardinality m that is comparable to n, the R2-ROC method identifies a surrogate solution for any specific parameter $\boldsymbol{\mu}$ in the following form:

$$\widehat{u}_n(\boldsymbol{\mu}) = W_n\boldsymbol{c}_n(\boldsymbol{\mu}).$$

Here, for simplicity of notation, we also adopt W_n for the snapshot matrix whose column space forms the reduced space W_n. We subject this surrogate solution to the FOM equation (2.10) which encompasses (2.5), (2.6), (2.8), and (2.9). Note, however, that $\widehat{u}_n(\boldsymbol{\mu})$ automatically satisfies the uniqueness condition (2.8) due to the fact that the constraint

$$\frac{\sum_{\boldsymbol{x}_\theta \in X^{\mathcal{N}}} \widehat{u}_n(\boldsymbol{x}_\theta;\boldsymbol{\mu})}{\mathcal{N}} \equiv 0$$

is linear and that all RB snapshots $\{u_i\}_{i=1}^n$ satisfy it by definition. Therefore, we just need to subject $\widehat{u}_n(\boldsymbol{\mu})$ to (2.5), (2.6), and (2.9) written as a nonlinear system, the ROM counterpart of the FOM equation (2.10):

$$F_r(W_n\boldsymbol{c}_n(\boldsymbol{\mu}), \sigma(\boldsymbol{\mu}); \phi^k(X^{\mathcal{N}} \cap \partial X;\boldsymbol{\mu})) = 0, \tag{3.1}$$

with $\mathcal{N}$ equations for unknown $(\boldsymbol{c}_n(\boldsymbol{\mu}), \sigma(\boldsymbol{\mu}))^T$. The kth iterate of the solution, $\boldsymbol{c}_n^k(\boldsymbol{\mu}) \in \mathbb{R}^{n\times 1}$ and $\sigma^k(\boldsymbol{\mu})$, is obtained by minimizing a subsampled residual

$$(\boldsymbol{c}_n^k(\boldsymbol{\mu}), \sigma^k(\boldsymbol{\mu}))^T = \underset{\boldsymbol{c}_n\in\mathbb{R}^{n\times 1}, \sigma\in\mathbb{R}}{\arg\min} \left\| P_*\left(F_r(W_n\boldsymbol{c}_n(\boldsymbol{\mu}), \sigma(\boldsymbol{\mu}); \phi^k(X^{\mathcal{N}} \cap \partial X;\boldsymbol{\mu}))\right)\right\|_{\ell^2(\mathbb{R}^m)}.$$

We note that, just like the transport boundary condition (2.7) was enforced on the FOM level numerically being replaced by a sequence of discretized Neumann boundary conditions (2.9) which is embedded in (2.10), the transport boundary condition is also enforced on the ROM level by (3.1). The Neumann boundary data $\phi(X^m \cap \partial X;\boldsymbol{\mu})$ is corrected at every iteration through projecting the RB mapping $\nabla_h\widehat{u}_n(\boldsymbol{\mu})(X^m\cap\partial X;\boldsymbol{\mu})$ to ∂Y. Along the same notion, just like the boundary ∂X will not be transported exactly to ∂Y (with an error at the level of the FOM accuracy), the transported ∂X will also differ from ∂Y on the ROM level by an error at the ROM level, as confirmed by our numerical experiments.

We also note that, in this paper, we focus on the parameterized Monge–Ampère equation with parameters describing the variation of the densities. While the variation of the density near the boundary may lead to the change of the mapping at the boundary, which is reflected by the function $\phi(X^{\mathcal{N}} \cap \partial X;\boldsymbol{\mu})$, the parameters do not directly delineate any boundary deformations. Any low-rank structure of the density function with respect to the parameter $\boldsymbol{\mu}$ translates to one for the boundary function $\phi(X^{\mathcal{N}} \cap \partial X;\boldsymbol{\mu})$. This is another insight that the low-dimensional RB approximation is capable of deriving a reliable mapping from ∂X to ∂Y even between polygonal and curved boundaries, as shown by our numerical experiments.

The RB space W_n, the reduced collocation set X^m, and the subsampling matrix $P_* \in \mathbb{R}^{m\times\mathcal{N}}$ that is constructed according to X^m will be generated in the offline process that is described next. The online algorithm is presented in Algorithm 3.1.

Online efficiency and robustness with respect to the shortest-distance projection $\mathbb{P}_{\partial Y}$. The RB method is said to be online-efficient if the RB solver can be assembled and the RB approximation solved in complexity independent of $\mathcal{N}$ in the online stage and the error estimator can be computed, via an offline-online decomposition if necessary, in complexity independent of $\mathcal{N}$ online [11]. The R2-ROC method is online-efficient as established in [14]. Our version of the R2-ROC method for solving the parameterized Monge–Ampère equation with a transport boundary features the added layer of iteration and the shortest-distance projection $\mathbb{P}_{\partial Y}$ in (2.3). We note that the iteration is up to a fixed number K and that $\mathbb{P}_{\partial Y}$ is only carried out for part of the boundary points, $S^k(\boldsymbol{\mu})\,(\subset X^{\mathcal{N}} \cap \partial X)$, whose cardinality only depends on m. Therefore, we conclude that our R2-ROC method remains online-efficient.

Moreover, we emphasize that the shortest-distance projection $\mathbb{P}_{\partial Y}(\nabla u^k(\boldsymbol{x};\boldsymbol{\mu}))$ at each iteration must be calculated exactly whenever possible. If, for example, it is done via a simple search algorithm on the discrete points of boundary ∂Y (discretizing ∂Y by $\partial Y_{\mathcal{N}}$ and calculating $\mathbb{P}_{\partial Y}(\boldsymbol{v})$ as $\arg\min_{\boldsymbol{y}\in\partial Y_{\mathcal{N}}}\|\boldsymbol{y}-\boldsymbol{v}\|$), the truth solver and

Algorithm 3.1 Online algorithm: the reduced algorithm for the transport boundary value problem of Monge–Ampère equation

```
Set $\phi^{-1}(\boldsymbol{x};\boldsymbol{\mu}) = B\boldsymbol{x}\cdot\boldsymbol{n}$ for sufficient large $B$, the error tolerance $\epsilon$, and the maximum number of iterations $K$. Compute $(\boldsymbol{c}_n^0(\boldsymbol{\mu}), \sigma^0(\boldsymbol{\mu}))^T$ by solving $P_* F_r(W_n \boldsymbol{c}_n(\boldsymbol{\mu}), \sigma(\boldsymbol{\mu}); \phi^{-1}(X^{\mathcal{N}} \cap \partial X; \boldsymbol{\mu})) = 0$.
Initialize $k = 0$ and $r = 1$.
while $r \geq \epsilon$ and $k < K$ do
    Compute $\phi^k(\boldsymbol{x}_\theta;\boldsymbol{\mu}) = \mathbb{P}_{\partial Y}(\nabla_h \widehat{u}_n^k(\boldsymbol{\mu})(\boldsymbol{x}_\theta;\boldsymbol{\mu}))\cdot\boldsymbol{n}$ for some $\boldsymbol{x}_\theta \in S^k(\boldsymbol{\mu})$, where $\widehat{u}_n^k(\boldsymbol{\mu}) = W_n \boldsymbol{c}_n^k(\boldsymbol{\mu})$.
    Compute $(\boldsymbol{c}_n^{k+1}(\boldsymbol{\mu}), \sigma^{k+1}(\boldsymbol{\mu}))^T$ by solving
        $\left\| P_* F_r(W_n \boldsymbol{c}_n(\boldsymbol{\mu}), \sigma(\boldsymbol{\mu}); \phi^k(X^{\mathcal{N}} \cap \partial X; \boldsymbol{\mu})) \right\|_{\ell^2(\mathbb{R}^m)} = 0.$
    Compute the relative error $r = \left\| \boldsymbol{c}_n^{k+1}(\boldsymbol{\mu}) - \boldsymbol{c}_n^k(\boldsymbol{\mu}) \right\|_{\ell^\infty(\mathbb{R}^n)}$.
    Let $k = k + 1$.
end while
```

our reduced solver, albeit feasible, are both less robust. The exact projection is straightforward when, for example, the target boundary ∂Y is a polygon or a circle. Appropriate projections do exist for less straightforward geometries such as the ellipses [42, 27].

Offline training. The offline component utilizes the classical parameter-greedy framework with an error indicator based on the hyper-reduced residual [14] to iteratively construct the RB space W_n and subsequently enrich the collocation set X^m, which determines the subsampling matrix P_*. The algorithm judiciously identifies parameter values $\left\{\boldsymbol{\mu}^1, \ldots, \boldsymbol{\mu}^N\right\}$ one by one and constructs the RB space via the corresponding snapshots. With these notations set, we start the greedy procedure with a randomly chosen $\boldsymbol{\mu}^1$ and obtain the snapshots $u^{\mathcal{N}}(X^{\mathcal{N}};\boldsymbol{\mu}^1)$ by the high fidelity algorithm. The RB space W_1 is then set as $W_1 = \{u_1\} = \{u^{\mathcal{N}}(X^{\mathcal{N}};\boldsymbol{\mu}^1)\}$, and the first collocation point is chosen as the EIM point of the first basis $\boldsymbol{x}_\star^1 = \arg\max_{x \in X^{\mathcal{N}}} |u_1|$. In addition, we add a collocation point, $\boldsymbol{x}_\star^0 = \arg\max_{\boldsymbol{x}_\theta \in X^{\mathcal{N}}} |u^{\mathcal{N}}(\boldsymbol{x}_\theta;\boldsymbol{\mu}^1) - u^{\mathcal{N}}(\boldsymbol{x}_\star^1;\boldsymbol{\mu}^1)|$, to guarantee the well-posedness of the RB problem. We then use the online procedure described above to obtain an RB approximation $\widehat{u}_n(\boldsymbol{\mu})$ for each parameter $\boldsymbol{\mu}$ in Ξ_{train} (a discretization of the parameter domain $\mathcal{D}$) and compute its error indicator $\Delta_n^{RR}(\boldsymbol{\mu})$:

$$\Delta_n^{RR}(\boldsymbol{\mu}) \coloneqq \|P_* r_n(\boldsymbol{\mu})\|_{\ell^\infty(\mathbb{R}^m)}, \quad \text{where}$$

$$r_n(\boldsymbol{\mu}) = F_r(W_n \boldsymbol{c}_n^{K_n(\boldsymbol{\mu})}(\boldsymbol{\mu}), \sigma^{K_n(\boldsymbol{\mu})}(\boldsymbol{\mu}); \phi^{K_n(\boldsymbol{\mu})-1}(X^{\mathcal{N}} \cap \partial X; \boldsymbol{\mu}))$$

is the *full* residual for the current RB approximation $\widehat{u}_n(\boldsymbol{\mu})$ of parameter $\boldsymbol{\mu}$, and $K_n(\boldsymbol{\mu})$ is the corresponding number of Neumann boundary iterations. $P_* r_n(\boldsymbol{\mu}) \in \mathbb{R}^{m\times 1}$ then represents its *reduced* (subsampled) version,[2] whose evaluation is independent of $\mathcal{N}$. After these error indicators are evaluated, we proceed as follows to enrich the RB space and expand the collocation sets.

---

[2] The conventional error estimate calculates the negative order norm of the residual and scales it by the (parametric) stability factor. It is challenging to compute the nonlinear and nonaffine cases with an EIM expansion due to the involvement of the successive constraint method [39, 40] used to efficiently estimate the parametric stability factor and the delicacy of evaluating the residual norm even for the linear problem [11, 17]. This simple error indicator based on the reduced residual [14] has shown to be promising for nonlinear and nonaffine problems without the need of EIM expansion.

1. *Greedy in μ:* The greedy choice is through maximizing $\Delta_n^{RR}(\boldsymbol{\mu})$ over the training set Ξ_{train}:
$$\boldsymbol{\mu}^{n+1} = \underset{\boldsymbol{\mu}\in\Xi_{\text{train}}}{\arg\max}\,\Delta_n^{RR}(\boldsymbol{\mu}). \tag{3.2}$$
2. *X^m expansion:* With the newly selected $\boldsymbol{\mu}^{n+1}$, we solve for the truth approximations $u_{n+1} = u^{\mathcal{N}}(X^{\mathcal{N}}; \boldsymbol{\mu}^{n+1})$. We then obtain the first additional collocation point from the EIM process of u_{n+1} and the second additional point by the EIM process of the full residual $r_n(\boldsymbol{\mu}^{n+1})$.

The offline algorithm of the ROC method is shown in Algorithm 3.2. We next provide more details on two aspects of this algorithm, namely the role of the two sets of collocation points, and the effectivity of the hyper-reduced error indicator.

Algorithm 3.2 Offline algorithm: the reduced over-collocation methods for the transport boundary value problem of Monge–Ampère equation

```
Choose $\boldsymbol{\mu}^1$ randomly in $\Xi_{\text{train}}$, and obtain $u^{\mathcal{N}}(\boldsymbol{\mu}^1)$ by Algorithm 2.1. Find $\boldsymbol{x}_\star^1 = \arg\max_{\boldsymbol{x}_\theta\in X^{\mathcal{N}}} |u^{\mathcal{N}}(\boldsymbol{x}_\theta;\boldsymbol{\mu}^1)|$ and $\boldsymbol{x}_\star^0 = \arg\max_{\boldsymbol{x}_\theta\in X^{\mathcal{N}}} |u^{\mathcal{N}}(\boldsymbol{x}_\theta;\boldsymbol{\mu}^1) - u^{\mathcal{N}}(\boldsymbol{x}_\star^1;\boldsymbol{\mu}^1)|$. Then let $n = 1$, $m = 2$, $X_s^n = \{\boldsymbol{x}_\star^1\}$, $X^m = X_s^n \cup \boldsymbol{x}_\star^0$, and $u_1 = u^{\mathcal{N}}(\boldsymbol{\mu}^1)/u^{\mathcal{N}}(\boldsymbol{x}_\star^1;\boldsymbol{\mu}^1)$.
Initialize $W_1 = \{u_1\}$ and $X_r^0 = \emptyset$.
for $n = 2, \dots, N$ do
    Solve $\boldsymbol{c}_{n-1}(\boldsymbol{\mu})$ by Algorithm 3.1 with $W_{n-1}, X^m$, and calculate $\Delta_{n-1}^{RR}$ for every $\boldsymbol{\mu} \in \Xi_{\text{train}}$.
    Find $\boldsymbol{\mu}^n = \arg\max_{\boldsymbol{\mu}\in\Xi_{\text{train}}} \Delta_{n-1}^{RR}(\boldsymbol{\mu})$.
    Solve $u_n := u^{\mathcal{N}}(\boldsymbol{\mu}^n)$ by Algorithm 2.1. Orthogonalize $u_n$: find $\{\alpha_j\}$, and let $u_n = u_n - \sum_{j=1}^{n-1} \alpha_j u_j$ such that $u_n(X_s^{n-1}) = 0$.
    Find $\boldsymbol{x}_\star^n = \arg\max_{\boldsymbol{x}_\theta\in X^{\mathcal{N}}} |u_n(\boldsymbol{x}_\theta)|$, $u_n = u_n/u_n(\boldsymbol{x}_\star^n)$, and let $X_s^n = X_s^{n-1} \cup \{\boldsymbol{x}_\star^n\}$.
    Assume that $\sigma(\boldsymbol{\mu}^n), \phi(X^{\mathcal{N}} \cap \partial X; \boldsymbol{\mu}^n)$ are obtained when solving $\boldsymbol{c}_{n-1}(\boldsymbol{\mu}^n)$ in step 5 of Algorithm 3.1. Then compute the full residual vector $r_{n-1} = F_1(W_{n-1}\boldsymbol{c}_{n-1}(\boldsymbol{\mu}^n), \sigma(\boldsymbol{\mu}^n); \phi(X^{\mathcal{N}} \cap \partial X; \boldsymbol{\mu}^n))$ and orthogonalize $r_{n-1}$: find $\{\alpha_j\}$, and let $r_{n-1} = r_{n-1} - \sum_{j=1}^{n-2} \alpha_j r_j$ such that $r_{n-1}(X_r^{n-2}) = 0$.
    Find $\boldsymbol{x}_{\star\star}^{n-1} = \arg\max_{\boldsymbol{x}_\theta\in \boldsymbol{x}^{\mathcal{N}}} |r_{n-1}(\boldsymbol{x}_\theta)|$. Let $r_{n-1} = r_{n-1}/r_{n-1}(\boldsymbol{x}_{\star\star}^{n-1})$ and $X_r^{n-1} = X_r^{n-2} \cup \{\boldsymbol{x}_{\star\star}^{n-1}\}$.
    Update $W_n = [W_{n-1}, u_n]$, $X^m = X_s^n \cup X_r^{n-1} \cup \boldsymbol{x}_\star^0$.
end for
```

The role of the two sets of collocation points. The role of the two sets of points, one from the snapshots and the other from the residual of their corresponding RB approximations when the RB space is one dimension less,

$$r_{n-1} = F_r(W_{n-1}\boldsymbol{c}_{n-1}(\boldsymbol{\mu}^n), \sigma(\boldsymbol{\mu}^n); \phi(X^{\mathcal{N}} \cap \partial X; \boldsymbol{\mu}^n)),$$

is to collectively produce accurate and stable representations for both the reduced solutions and the residuals at other parameter values. The first set of points, consisting of the maximizers from an EIM process of the RB functions [13, 14], is denoted by $X_s^n = \{\boldsymbol{x}_\star^i\}_{i=1}^n$. The basis functions, together with these points, lead to a stable and accurate interpolation procedure with slow growth in Lebesgue constant [3, 33] for the truth approximations $u^{\mathcal{N}}(\boldsymbol{\mu})$. These truth approximations are of course not accessible by the ROM solver, which, instead of interpolation, looks for the element in the RB space, for each $\boldsymbol{\mu}$, that minimizes the (subsampled) residual when it is subject to the

PDE corresponding to that $\boldsymbol{\mu}$. It is therefore critical to represent these residuals well. This goal is achievable with only the first set of points for simple linear equations [13], but it is out of reach for nonlinear or linear but degenerate cases [15]. Therefore, we introduce the second set of points to better control the residual of the numerical PDE at the ROM level. The residual vectors corresponding to the snapshots $\{r_{n-1}\}_{n=2}^{N}$ serve naturally as a set of basis functions for representing a generic residual $r_n(\boldsymbol{\mu})$. Their EIM interpolation points $X_r^{n-1} = \{x_{\star\star}^i\}_{i=1}^{n-1}$ are then introduced as the second part of our over-collocation set. Analysis of [14] demonstrates the optimality of these two sets of points for the purpose of representing the RB solution and controlling the residuals, respectively. Given an error-residual relation, the ROC solution will produce accurate surrogate solutions.

Remark 3.1. In [14], the first set of points consisting of the interpolation points for the truth solution is produced by the generalized EIM (GEIM) process which, due to its adoption of the discrete PDE operator, leads to the mentioned optimality. The strong nonlinearity of the Monge–Ampère equation makes it difficult for us to directly exploit the approach of [14]. Our first set of points is instead obtained from the (weaker) interpolation process that does not consider any discrete PDE operators.

Effectivity of the hyper-reduced error indicator. The efficiency of our hyper-reduced error indicator Δ_n^{RR} is apparent thanks to the low-cost evaluation that is independent of $\mathcal{N}$ and the number of EIM expansion terms. Its effectivity is entirely dependent on the choice of the over-collocation points. As a reference, we introduce the error estimator based on the full residual

$$\Delta_n^R(\boldsymbol{\mu}) = \|r_n(\boldsymbol{\mu})\|_{\ell^\infty(\mathbb{R}^{\mathcal{N}})}.$$

Given a residual to error map and a nonoscillatory (with respect to the parameter) stability factor, it can serve as a reliable estimator with a near-constant effectivity index [38, 53]. However, we note that this estimator is not online efficient, as it is dependent on $\mathcal{N}$. If, for example, the maximizers of $\|r_n(\boldsymbol{\mu})\|$ over the full grid are contained in $X_s^n \bigcup X_r^{n-1}$ or $\Delta_n^R(\boldsymbol{\mu})$ is bounded above and below by $\Delta_n^{RR}(\boldsymbol{\mu})$, our hyper-reduced error indicator will be equally reliable. Although we do not have such proofs, our numerical examples in section 4.2 (Figure 5) indicate that our hyper-reduced version $\Delta_n^{RR}(\boldsymbol{\mu})$ is very much comparable to $\Delta_n^R(\boldsymbol{\mu})$.

4. Numerical results.

In this section, we present the computational results to verify two main works of this paper: the proposed narrow-stencil FDM is effective in solving the transport boundary problem of the Monge–Ampère equation, and the adapted R2-ROC method can efficiently solve the parameterized transport boundary problem.

4.1. FDM results.

In this section, we focus on our Monge–Ampère equation solver. The results of four tests are presented to gauge the performance of the proposed approach for approximating the viscosity solutions. The problems are described in Table 1, which lists the original density $f_X(\boldsymbol{x})$, the target density $f_Y(\boldsymbol{y})$, and the exact mapping $\nabla_{\boldsymbol{x}} u$. The first one maps the square $(-0.5, 0.5) \times (-0.5, 0.5)$ onto the rectangle$(0.5, 1.5) \times (-0.25, 0.25)$. The second test maps the density

$$f_X(\boldsymbol{x}) = 1+4(q''(x_1)q(x_2)+q(x_1)q''(x_2))+16(q(x_1)q(x_2)q''(x_1)q''(x_2)-q'(x_1)^2q'(x_2)^2)$$

on the square $(-0.5, 0.5) \times (-0.5, 0.5)$ onto a uniform density on the same square with the auxiliary function $q(z)$ defined as follows:

$$q(z) = \left(-\frac{1}{8\pi} z^2 + \frac{1}{256\pi^3} + \frac{1}{32\pi} \right) \cos(8\pi z) + \frac{1}{32\pi^2} z \sin(8\pi z).$$

The third one maps a uniform density on the unit square $(0, 1) \times (0, 1)$ onto a density that blows up at a point on the same square. The last one maps a uniform density on the square $(-0.5, 0.5) \times (-0.5, 0.5)$ onto a Gaussian density on the disk $y_1^2 + y_2^2 \leq 1$. This last test is meant to verify the effectiveness of our approach for transporting a rectangular boundary to a circular one, a nontrivial task.

TABLE 1

Setup of the test problems for the transport boundary case.

Test	Original density	Target density	Exact mapping
1	$f_X(\boldsymbol{x}) = \frac{1}{0.16} \exp\left(-\frac{1}{2} \frac{x_1^2}{0.4^2} - \frac{1}{2} \frac{x_2^2}{0.4^2} \right)$	$f_Y(\boldsymbol{y}) = \frac{1}{0.08} \exp\left(-\frac{1}{2} \frac{(y_1-1)^2}{0.4^2} - \frac{1}{2} \frac{y_2^2}{0.2^2} \right)$	$\nabla_{\boldsymbol{x}} u = (x_1 + 1, \frac{x_2}{2})$
2	$f_X(\boldsymbol{x}) = 1 + 4(q''(x_1)q(x_2) + q(x_1)q''(x_2)) +$ $16(q(x_1)q(x_2)q''(x_1)q''(x_2) - q'(x_1)^2 q'(x_2)^2)$	1	$u_{x_1} = x_1 + 4q'(x_1)q(x_2)$ $u_{x_2} = x_2 + 4q'(x_2)q(x_1)$
3	1	$f_Y(\boldsymbol{y}) = \frac{\exp(-2\sqrt{(y_1-0.5)^2+(y_2-0.5)^2})}{\sqrt{(y_1-0.7)^2+(y_2-0.7)^2}}$	-
4	1	$f_Y(\boldsymbol{y}) = 1 + \frac{1}{0.02\pi} \exp\left(-\frac{y_1^2+y_2^2}{0.02} \right)$	-

We present the result in Table 2. Here, the maximum errors are computed based on the exact solutions or the solutions on the finest grids. From the table, we can see the solutions indeed achieve machine accuracy for the first test and order 2 accuracy for the second, even without α and β. For the third, many currently available methods become slow or unstable when the ratio $R = \min\{\frac{f_X(\boldsymbol{x})}{f_Y(\nabla u(\boldsymbol{x}))}\}$ is small. We see that our approach works well with small α, even when R is very small. We also provide in Figure 2 a uniform Cartesian mesh and its images under the second, third, and fourth maps.

TABLE 2

The number of iterations, CPU time, error of numerical solution, and order with respect to $\mathcal{N}$ for the transport boundary case.

$\mathcal{N}$	Test 1 ($\alpha = \beta = 0$)		Test 2 ($\alpha = \beta = 0$)			Test 3 ($\alpha = 1, \beta = 0$)				Test 4 ($\alpha = 10, \beta = 0$)			
	time(s)	max error	time(s)	max error	order	R	time(s)	max error	order	iteration	time(s)	max error	order
15^2	0.48	2.44E-15	0.05	2.72E-03	–	1.92E-02	0.07	7.18E-02	–	20	0.85	2.81E-01	–
31^2	0.11	5.88E-15	0.06	7.47E-04	1.78	3.19E-03	0.13	3.08E-02	1.17	22	2.27	2.20E-01	0.33
65^2	0.75	7.11E-15	0.51	2.24E-04	1.63	8.39E-04	1.23	1.10E-02	1.40	21	17.02	1.30E-01	0.72
127^2	7.71	2.89E-14	3.77	6.18E-05	1.92	1.55E-04	10.39	4.14E-03	1.45	20	173.45	5.39E-02	1.31
255^2	90.70	5.68E-14	51.55	1.55E-05	1.98	2.00E-04	130.04	1.23E-03	1.75	21	2331.48	1.39E-02	1.95
511^2	2789.93	7.17E-14	1676.06	3.88E-06	2.00	8.08E-05	2052.19	–	–	21	93834.32	–	–

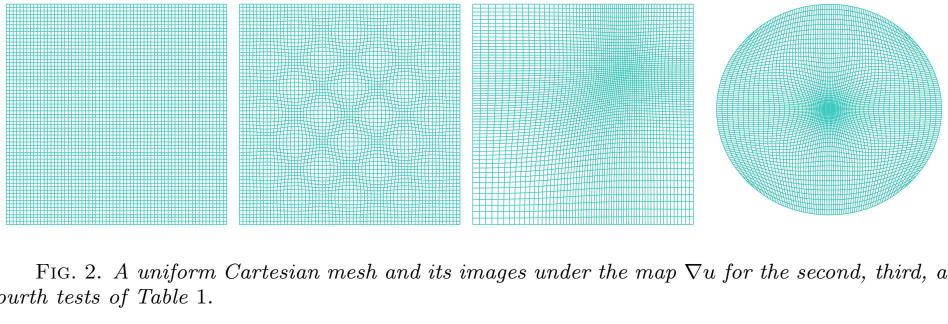

FIG. 2. *A uniform Cartesian mesh and its images under the map ∇u for the second, third, and fourth tests of Table 1.*

4.2. RBM results for the parameterized transport boundary problem.

In this section, we present numerical results for the following five problems to demonstrate the applicability and the efficiency of the R2-ROC method for the parameterized transport boundary problem of the Monge–Ampère equation.

RB-Test 1. Transporting the following density to a uniform density on the square $(-0.5, 0.5)^2$:

$$f_X(\boldsymbol{x}, \mu) = 1 + 4(q''_\mu(x_1)q_\mu(x_2) + q_\mu(x_1)q''_\mu(x_2)) + 16(q_\mu(x_1)q_\mu(x_2)q''_\mu(x_1)q''_\mu(x_2) - q'_\mu(x_1)^2 q'_\mu(x_2)^2),$$

where the auxiliary function is given by $q_\mu(z) = (-\frac{1}{\mu\pi}z^2 + \frac{1}{32\mu\pi^3} + \frac{1}{4\mu\pi})\cos(8\pi z) + \frac{1}{4\mu\pi^2} z\sin(8\pi z)$ and the exact solution is provided as

$$\nabla u = (x_1 + 4q'(x_1, \mu)q(x_2, \mu),\ x_2 + 4q'(x_2, \mu)q(x_1, \mu))\,.$$

RB-Test 2. Transporting a uniform density to a density that blows up at a moving point (μ_1, μ_2) on the square $(0, 1)^2$:

$$f_Y(\boldsymbol{y}, \boldsymbol{\mu}) = \frac{\exp(-2\sqrt{(y_1 - 0.5)^2 + (y_2 - 0.5)^2})}{\sqrt{(y_1 - \mu_1)^2 + (y_2 - \mu_2)^2}}.$$

RB-Test 3. Transporting a uniform density to the following density function on the square $(0, 1)^2$:

$$f_Y(\boldsymbol{y}, \mu) = 1 + 5\exp(-50|(y_1 - 0.5 - \mu)^2 + (y_2 - 0.5)^2 - 0.09|).$$

RB-Test 4. Transporting a uniform density to the following density function on the square $(0, 1)^2$:

$$f_Y(\boldsymbol{y}, \mu) = 1 + 5\exp(-50|(y_1 - 0.5 - 0.25\cos(2\pi\mu))^2 + (y_2 - 0.5 - 0.25\cos(2\pi\mu))^2 - 0.01|).$$

RB-Test 5. Transporting a uniform density on the square $(-0.5, 0.5)^2$ to the following density on the disk $y_1^2 + y_2^2 \leq 1$:

$$f_Y(\boldsymbol{y}, \mu) = 1 + \exp\left(-\frac{y_1^2 + y_2^2}{2\mu^2}\right)/(2\pi\mu^2).$$

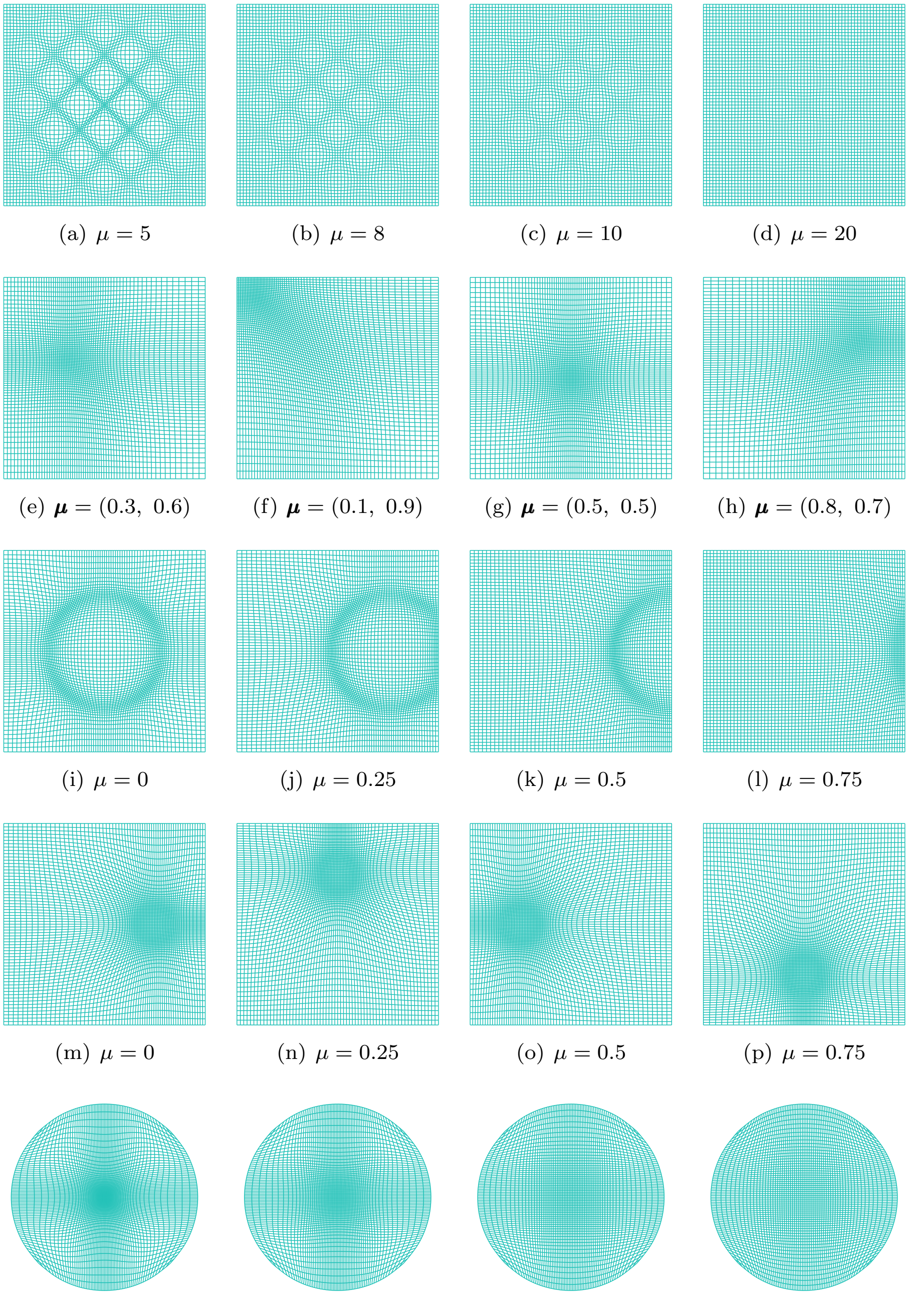

(a) $\mu = 5$ (b) $\mu = 8$ (c) $\mu = 10$ (d) $\mu = 20$

(e) $\boldsymbol{\mu} = (0.3,\ 0.6)$ (f) $\boldsymbol{\mu} = (0.1,\ 0.9)$ (g) $\boldsymbol{\mu} = (0.5,\ 0.5)$ (h) $\boldsymbol{\mu} = (0.8,\ 0.7)$

(i) $\mu = 0$ (j) $\mu = 0.25$ (k) $\mu = 0.5$ (l) $\mu = 0.75$

(m) $\mu = 0$ (n) $\mu = 0.25$ (o) $\mu = 0.5$ (p) $\mu = 0.75$

(q) $\mu = 0.1$ (r) $\mu = 0.14$ (s) $\mu = 0.19$ (t) $\mu = 0.24$

FIG. 3. *The image of the truth solutions at representative parameter values for RB-Tests* 1–5 *of Table* 3 *(from top to bottom).*

Figure 3 shows the truth approximations at representative parameter values that are generated with the narrow-stencil FDM on a mesh of size $\mathcal{N} = 127^2$ and (α, β) values given in Table 3. Parametric variations are clearly visible for each example. In particular, we aim to capture a moving singular point for RB-Test 2, a circle of denser measure moving to the right for RB-Test 3, and a nontrivial task of transporting a rectangular boundary to a circular one in RB-Test 5.

Table 3
Test problem setup for the parametric transport boundary case.

RB-Test	(α, β)	Ξ_{train}	Ξ_{test}
1	$(0, 0)$	$(5 : 0.2 : 20)$	$(5.1 : 0.2 : 19.9)$
2	$(200, 0)$	$(0.1 : 0.04 : 0.9)^2$	$(0.13 : 0.08 : 0.89)^2$
3	$(50, 0)$	$(0 : 0.02 : 1)$	$(0.01 : 0.02 : 9)$
4	$(50, 0)$	$(0 : 0.02 : 1)$	$(0.01 : 0.02 : 9)$
5	$(10, 0)$	$(0.1 : 0.01 : 0.3)$	$(0.105 : 0.01 : 0.295)$

For these calculations, the error tolerance ϵ is 10^{-8}, and the maximum number of iterations K is 100. Using the training and testing sets specified in Table 3 for the R2-ROC method, we generate the RB space and the collocation set, with which we compute the RB solution $\widehat{u}_N(\boldsymbol{\mu})$, where N is the number of basis functions that we used. To test the R2-ROC method, we compute the maximum error $E(N)$ between the mappings induced by the RB solution $\widehat{u}_N(\boldsymbol{\mu})$ and the truth approximation $u^{\mathcal{N}}(\boldsymbol{\mu})$ for all $\boldsymbol{\mu} \in \Xi_{\text{test}}$. That is,

$$E(N) = \max_{\boldsymbol{\mu} \in \Xi_{\text{test}}} \left\{ ||\nabla_h u^{\mathcal{N}}(\boldsymbol{\mu}) - \nabla_h \widehat{u}_N(\boldsymbol{\mu})||_{\ell^\infty(\mathbb{R}^{\mathcal{N}})} \right\}.$$

The left column of Figure 5 shows the maximum errors that are plotted against the number of basis functions. Exponential convergence is observed in all cases. RB-Tests 2–4 are challenging due to moving singularities (i.e., the regions of low regularity vary with the parameter $\boldsymbol{\mu}$). The convergence is noticeably slower. The same can be seen for RB-Test 5, featuring a more challenging transport from a rectangular to a nonrectangular target domain. However, it is clearly still worthwhile to invest in the offline process of the R2-ROC for all cases, even when only a modest number of inquiries are needed. To verify the capability of the ROM solver in transporting the boundary, we pick a boundary point on the square boundary ∂X of the most challenging case, RB-Test 5, and examine how it is transported to the circle ∂Y when the parameter value $\boldsymbol{\mu} = 0.135$. We record the distance between the ROM target point (transported by $\nabla_h \widehat{u}_N(\boldsymbol{\mu})$) and the FOM target point (transported by $\nabla_h u^{\mathcal{N}}(\boldsymbol{\mu})$) as the Neumann boundary iteration proceeds and we vary the ROM dimension $N = 2, 4, 6, 8$. The histories of convergence of this distance for the picked point, all boundary points, and grid points of the entire domain are displayed in Figure 4. It is clear that the sequence of ROM level Neumann boundary problems is highly effective in resolving the transport boundary. Moreover, the terminal accuracy improves as the RB spaces are enriched and they are at their expected ROM accuracy. Indeed, $\|u^{\mathcal{N}}(\boldsymbol{\mu}) - \widehat{u}_N(\boldsymbol{\mu})\|$ are at the $1E-01, 1E-03, 1E-04, 1E-04$ levels for $N = 2, 4, 6, 8$. The terminal errors for the entire domain, shown in Figure 4 (right), correspond well with the inverse inequality relating $\|\nabla_h (u^{\mathcal{N}}(\boldsymbol{\mu}) - \widehat{u}_N(\boldsymbol{\mu}))\|$ with $\|u^{\mathcal{N}}(\boldsymbol{\mu}) - \widehat{u}_N(\boldsymbol{\mu})\|$.

To demonstrate the efficiency, we compute the cumulative run time as a function of the number of queries N_{run} for the full and reduced solver with N basis, plotted

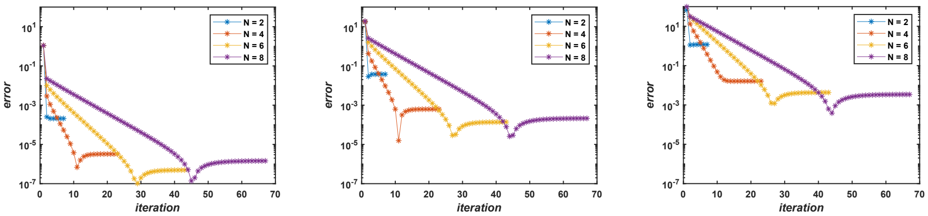

FIG. 4. *Test of ROM accuracy in transporting the boundary of RB-Test* 5 *(square to a circle). We measure the distance between the ROM target point (transported by $\nabla_h \widehat{u}_N(\boldsymbol{\mu})$) and the FOM target point (transported by $\nabla_h u^{\mathcal{N}}(\boldsymbol{\mu})$) as the Neumann boundary iteration proceeds and we vary the ROM dimension $N = 2, 4, 6, 8$. Shown in the figure are the histories of convergence of this distance for a fixed point (left), all boundary points (middle), and grid points of the entire domain (right).*

in the middle column of Figure 5. The offline cost is counted as an overhead for the reduced solver. We then evaluate the break-even number of queries $N^{\mathrm{e}}_{\mathrm{run}}$ above which it is more costly to run the full simulations for each query (and thus worthwhile to invest the overhead cost training the reduced solver). These quantities and the computation time of the R2-ROC method and the FOM are presented in Table 4. As we can see, the break-even numbers of queries $N^{\mathrm{e}}_{\mathrm{run}}$ are modest across the board thanks to the computation time of the R2-ROC online solver being hundreds of times smaller than that of the full solver.

TABLE 4
Offline and online computational times for different tests.

Test	N	N^e_{run}	R2-ROC		FDM
			Offline	Online	-
1	7	10	29.45	0.0091	3.18
2	20	30	193.24	0.011	6.76
3	15	17	118.53	0.0093	7.46
4	15	17	122.32	0.0088	8.21
5	10	12	1023.16	0.5303	90.24

4.3. Dirichlet boundary value problem of the Monge–Ampère equation.

For completeness, we test our methods on the Dirichlet boundary value problem of Monge–Ampère equation (2.1) and report the results in this section. In this case, the narrow-stencil FDM could be applied directly without the need of an iterative procedure for boundary enforcement. We consider three tests of decreasing regularities. Listed in Table 5 are their density function $f(\boldsymbol{x})$, exact solution $u(\boldsymbol{x})$ (which induces the boundary condition $g(\boldsymbol{x})$), and computational domain X. The relative L^∞ error between exact solution $u(\boldsymbol{x})$ and its approximation $u^{\mathcal{N}}(X^{\mathcal{N}})$, and its convergence orders together with the penalization parameters α and β, are presented in Table 6. This verifies that the method converges with the expected order of 2 when the first derivative is continuous.

To test our reduced order solver, we consider two parameterized Monge–Ampère equations listed in Table 7, corresponding to two of the nonparametric cases in Table 5. Truth approximations are generated with $\alpha = 1$ and $\beta = 0$ on a uniform Cartesian mesh of size $\mathcal{N} = 127^2$. Figure 6 shows two representative solutions for each example. For the first example, solutions for $\mu = 0.1$ and $\mu = 1$ differ the most around the $(1, 1)$-corner of the domain, while for the second example it is more challenging with

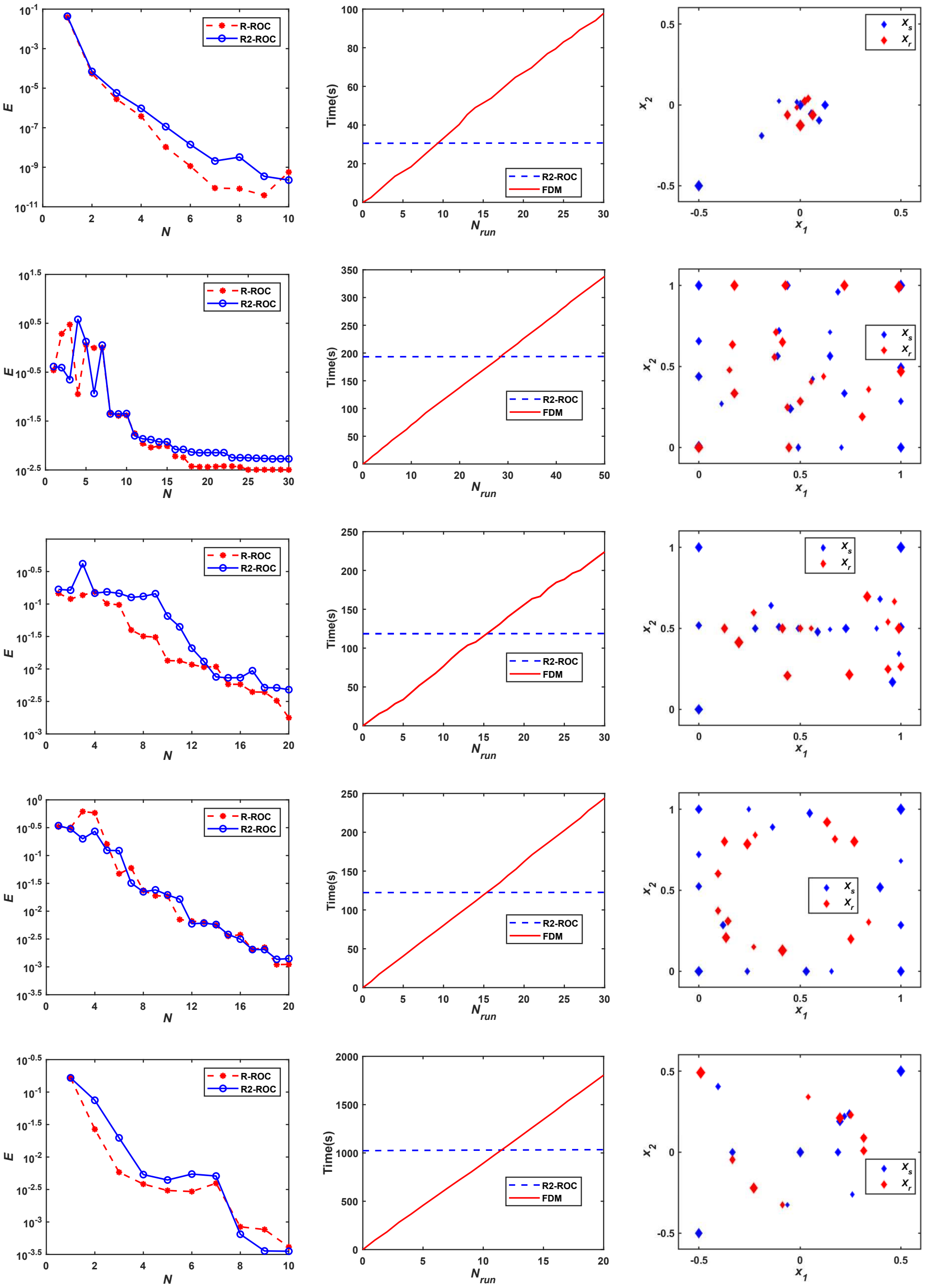

Fig. 5. *R2-ROC results for the parameterized transport boundary problem of the Monge–Ampère equation: the histories of convergence (left), comparison in cumulative run time (middle), and the collocation points for the R2-ROC method (right). On the top is for RB-Test* 1 *and the bottom for RB-Test* 5 *of Table* 3*.*

TABLE 5
Setup of the Dirichlet test problems.

Test	$(f(\boldsymbol{x}), u(\boldsymbol{x}))$	X
C^∞	$f(\boldsymbol{x}) = (1 + x_1^2 + x_2^2)\exp(x_1^2 + x_2^2)$ $u(\boldsymbol{x}) = \exp\left(\frac{x_1^2+x_2^2}{2}\right)$	$X = (0,1) \times (0,1)$
C^1	$f(\boldsymbol{x}) = \left(1 - \frac{0.2}{\lvert(x_1-0.5, x_2-0.5)\rvert}\right)^+$ $u(\boldsymbol{x}) = \frac{1}{2}((\lvert(x_1 - 0.5, x_2 - 0.5)\rvert - 0.2)^+)^2.$	$X = (0,1) \times (0,1)$
C^0	$f(\boldsymbol{x}) = 0$ $u(\boldsymbol{x}) = \lvert x_1\rvert$	$X = (-1,1) \times (-1,1)$

TABLE 6
Computation time, maximum error, and rates of convergence for the FDM solutions of the Dirichlet case.

$\mathcal{N}$	Test C^∞ $(\alpha = 1, \beta = 0)$			Test C^1 $(\alpha = 10, \beta = 0)$			Test C^0 $(\alpha = 200, \beta = 0)$		
	time(s)	error	order	time(s)	error	order	time(s)	error	order
15^2	0.03	8.98E-03	–	0.02	8.54E-02	–	0.02	1.14E-00	–
31^2	0.07	2.38E-03	1.83	0.05	2.07E-02	1.95	0.07	1.00E-00	0.19
65^2	0.63	5.97E-04	1.87	0.56	5.38E-03	1.82	0.63	4.92E-01	0.96
127^2	4.48	1.65E-04	1.92	5.52	3.05E-03	0.85	4.69	2.03E-01	1.32
255^2	45.74	4.28E-04	1.94	68.23	1.70E-03	0.84	80.14	1.04E-01	0.96
511^2	688.69	1.09E-05	1.96	1029.31	8.14E-04	1.06	–	–	–

the parameter μ dictating the location of the regularity change in the solution.

The R2-ROC results are presented in Figure 7. From the left column, we can see that the errors steadily decrease for the first test while it plateaus for the more challenging second test. The middle column displays the comparison in cumulative computation time for the R2-ROC method (with 15 bases for the first example and 7 for the second) and the finite difference method as we increase the number of simulations N_{run}. We see that the R2-ROC method starts to save time when the number of simulations is above 18 or 8 for the two tests, respectively, and that the savings become more dramatic as N_{run} increases due to the negligible marginal expense of R2-ROC.

TABLE 7
Setup of the test problems for the parametric Dirichlet case.

RB-Test	$(f(\boldsymbol{x}), u(\boldsymbol{x}))$	Ξ_{train}	Ξ_{test}
$C^\infty(\mu)$	$f(\boldsymbol{x}) = 4\mu^2(1 + 2\mu(x_1^2 + x_2^2))\exp(2\mu(x_1^2 + x_2^2))$ $u(\boldsymbol{x}) = \exp(\mu(x_1^2 + x_2^2))$	$(0.1 : 0.02 : 1)$	$(0.11 : 0.02 : 0.99)$
$C^1(\mu)$	$f(\boldsymbol{x}) = \left(1 - \frac{\mu}{\lvert(x_1-0.5, x_2-0.5)\rvert}\right)^+$ $u(\boldsymbol{x}) = \frac{1}{2}((\lvert(x_1 - 0.5, x_2 - 0.5)\rvert - \mu)^+)^2$	$(0.1 : 0.01 : .5)$	$(0.105 : 0.01 : 0.495)$

5. Conclusion. In this article, we develop a fast algorithm for the nonlinear parameterized Monge–Ampère equation with transport boundary, which models the optimal transport problem with L^2 cost function. It features a novel extension of the narrow-stencil finite difference scheme [23] to our setting, incorporating the projection-

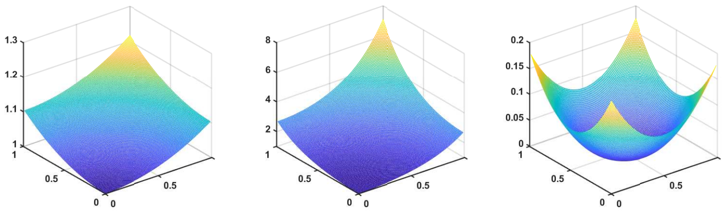

(a) $\mu = 0.1$ (b) $\mu = 1$ (c) $\mu = 0.1$

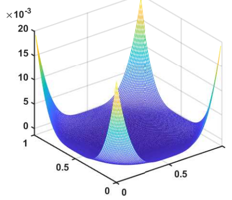

(d) $\mu = 0.5$

FIG. 6. *Truth solutions at representative parameter values for the $C^\infty(\mu)$ test ((a) and (b)) and the $C^1(\mu)$ test ((c) and (d)).*

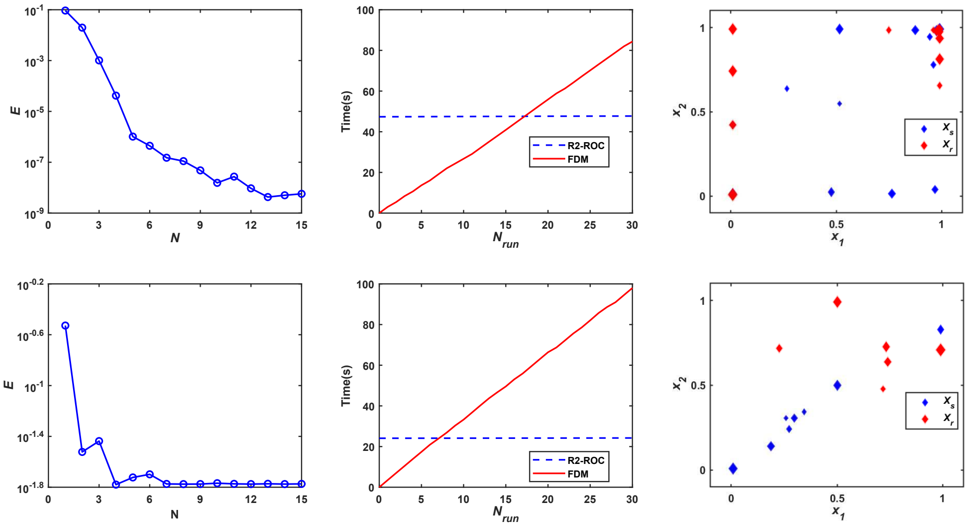

FIG. 7. *R2-ROC results for the parameterized Dirichlet boundary problem of the Monge–Ampère equation: the histories of convergence (left), comparison in cumulative run time (middle), and the collocation points for the R2-ROC method (right). On the top is for the $C^\infty(\mu)$ test and the bottom for the $C^1(\mu)$ test of Table 7.*

iteration method [27] to deal with the transport boundary. The resulting solver is shown to be effective and accurate even when facing low regularity. Building on this truth approximation solver, we adapt the R2-ROC algorithm [14, 16] to the parameterized Monge–Ampère equation with the transport boundary. Several challenging tests with different parameter delineations are provided to demonstrate the method's capability in efficiently producing an accurate and reliable mapping induced by the RB solution.

REFERENCES

[1] A. D. Aleksandrov, *Certain estimates for the Dirichlet problem*, Dokl. Akad. Nauk SSSR, 134 (1960), pp. 1001–1004 (in Russian); Soviet Math. Dokl., 1 (1961), pp. 1151–1154 (in English).

[2] M. Arjovsky, S. Chintala, and L. Bottou, *Wasserstein generative adversarial networks*, in Proceedings of the 34th International Conference on Machine Learning (ICML'17), Vol. 70, 2017, pp. 214–223.

[3] M. Barrault, Y. Maday, N. C. Nguyen, and A. T. Patera, *An "empirical interpolation" method: Application to efficient reduced-basis discretization of partial differential equations*, C. R. Math. Acad. Sci. Paris, 339 (2004), pp. 667–672.

[4] S. Basu, S. Kolouri, and G. K. Rohde, *Detecting and visualizing cell phenotype differences from microscopy images using transport-based morphometry*, Proc. Natl. Acad. Sci. USA, 111 (2014), pp. 3448–3453.

[5] J. D. Benamou and Y. Brenier, *A computational fluid mechanics solution to the Monge-Kantorovich mass transfer problem*, Numer. Math., 84 (2000), pp. 375–393.

[6] J. D. Benamou, B. D. Froese, and A. M. Oberman, *A Viscosity Solution Approach to the Monge-Ampere Formulation of the Optimal Transportation Problem*, preprint, https://arxiv.org/abs/1208.4873, 2012.

[7] L. Caffarelli, L. Nirenberg, and J. Spruck, *The Dirichlet problem for nonlinear second-order elliptic equations* I. *Monge-Ampère equation*, Comm. Pure Appl. Math., 37 (1984), pp. 369–402.

[8] L. A. Caffarelli, *Some regularity properties of solutions of Monge-Ampère equation*, Comm. Pure Appl. Math., 44 (1991), pp. 965–969.

[9] L. A. Caffarelli, *The regularity of mappings with a convex potential*, J. Amer. Math. Soc., 5 (1992), pp. 99–104.

[10] K. Carlberg, C. Farhat, J. Cortial, and D. Amsallem, *The GNAT method for nonlinear model reduction: Effective implementation and application to computational fluid dynamics and turbulent flows*, J. Comput. Phys., 242 (2013), pp. 623 – 647, https://doi.org/10.1016/j.jcp.2013.02.028.

[11] F. Casenave, A. Ern, and T. Lelièvre, *Accurate and online-efficient evaluation of the a posteriori error bound in the reduced basis method*, ESAIM Math. Model. Numer. Anal., 48 (2014), pp. 207–229.

[12] S. Chaturantabut and D. C. Sorensen, *Nonlinear model reduction via discrete empirical interpolation*, SIAM J. Sci. Comput., 32 (2010), pp. 2737–2764, https://doi.org/10.1137/090766498.

[13] Y. Chen and S. Gottlieb, *Reduced collocation methods: Reduced basis methods in the collocation framework*, J. Sci. Comput., 55 (2013), pp. 718–737.

[14] Y. Chen, S. Gottlieb, L. Ji, and Y. Maday, *An EIM-degradation free reduced basis method via over collocation and residual hyper reduction-based error estimation*, J. Comput. Phys., 444 (2021), 110545, https://doi.org/10.1016/j.jcp.2021.110545.

[15] Y. Chen, S. Gottlieb, and Y. Maday, *Parametric analytical preconditioning and its applications to the reduced collocation methods*, C. R. Math. Acad. Sci. Paris, 352 (2014), pp. 661–666, https://doi.org/10.1016/j.crma.2014.06.001.

[16] Y. Chen, L. Ji, A. Narayan, and Z. Xu, *L1-based reduced over collocation and hyper reduction for steady state and time-dependent nonlinear equations*, J. Sci. Comput., 87 (2021), 10.

[17] Y. Chen, J. Jiang, and A. Narayan, *A robust error estimator and a residual-free error indicator for reduced basis methods*, Comput. Math. Appl., 77 (2019), pp. 1963–1979.

[18] Y. Choi and K. Carlberg, *Space–time least-squares Petrov–Galerkin projection for nonlinear model reduction*, SIAM J. Sci. Comput., 41 (2019), pp. A26–A58, https://doi.org/10.1137/17M1120531.

[19] Y. Choi, D. Coombs, and R. Anderson, *SNS: A solution-based nonlinear subspace method for time-dependent model order reduction*, SIAM J. Sci. Comput., 42 (2020), pp. A1116–A1146, https://doi.org/10.1137/19M1242963.

[20] M. G. Crandall and P. L. Lions, *Two approximations of solutions of Hamilton-Jacobi equations*, Math. Comp., 43 (1984), pp. 1–19.

[21] T. A. El Moselhy and Y. M. Marzouk, *Bayesian inference with optimal maps*, J. Comput. Phys., 231 (2012), pp. 7815–7850.

[22] L. C. Evans, *Partial differential equations and Monge-Kantorovich mass transfer*, in Current Developments in Mathematics, 1997, International Press, Boston, MA, 1999, pp. 65–126.

[23] X. Feng and T. Lewis, *A Narrow-Stencil Finite Difference Method for Approximating Viscosity Solutions of Fully Nonlinear Elliptic Partial Differential Equations with Applications to Hamilton-Jacobi-Bellman Equations*, preprint, https://arxiv.org/abs/1907.10204, 2019.

[24] X. Feng and M. Neilan, *Mixed finite element methods for the fully nonlinear Monge–Ampère equation based on the vanishing moment method*, SIAM J. Numer. Anal., 47 (2009), pp. 1226–1250, https://doi.org/10.1137/070710378.

[25] X. Feng and M. Neilan, *Vanishing moment method and moment solutions for fully nonlinear second order partial differential equations*, J. Sci. Comput., 38 (2009), pp. 74–98.

[26] X. Feng and M. Neilan, *The Vanishing Moment Method for Fully Nonlinear Second Order Partial Differential Equations: Formulation, Theory, and Numerical Analysis*, preprint, https://arxiv.org/abs/1109.1183, 2011.

[27] B. D. Froese, *A numerical method for the elliptic Monge-Ampère equation with transport boundary conditions*, SIAM J. Sci. Comput., 34 (2012), pp. A1432–A1459, https://doi.org/10.1137/110822372.

[28] B. D. Froese and A. M. Oberman, *Convergent finite difference solvers for viscosity solutions of the elliptic Monge–Ampère equation in dimensions two and higher*, SIAM J. Numer. Anal., 49 (2011), pp. 1692–1714, https://doi.org/10.1137/100803092.

[29] C. Frogner, C. Zhang, H. Mobahi, M. Araya-Polo, and T. Poggio, *Learning with a Wasserstein Loss*, preprint, https://arxiv.org/abs/1506.05439, 2015.

[30] D. Gilbarg and N. S. Trudinger, *Elliptic Partial Differential Equations of Second Order*, Grundlehren Math. Wiss. 224, Springer, Berlin, New York, 1977.

[31] I. Goodfellow, Y. Bengio, and A. Courville, *Deep Learning*, MIT Press, Cambridge, MA, 2016.

[32] I. J. Goodfellow, J. Pouget-Abadie, M. Mirza, B. Xu, D. Warde-Farley, S. Ozair, A. Courville, and Y. Bengio, *Generative Adversarial Networks*, preprint, https://arxiv.org/abs/1406.2661, 2014.

[33] M. A. Grepl, Y. Maday, N. C. Nguyen, and A. T. Patera, *Efficient reduced-basis treatment of nonaffine and nonlinear partial differential equations*, ESAIM Math. Model. Numer. Anal., 41 (2007), pp. 575–605.

[34] C. E. Gutiérrez, *The Monge-Ampère Equation*, Progr. Nonlinear Differential Equations Appl. 44, Birkhäuser Boston, Boston, MA, 2001.

[35] B. Haasdonk, *Reduced basis methods for parametrized PDEs—a tutorial introduction for stationary and instationary problems*, in Model Reduction and Approximation, SIAM Philadelphia, 2017, pp. 65–136, https://doi.org/10.1137/1.9781611974829.ch2.

[36] E. Haber, T. Rehman, and A. Tannenbaum, *An efficient numerical method for the solution of the L_2 optimal mass transfer problem*, SIAM J. Sci. Comput., 32 (2010), pp. 197–211, https://doi.org/10.1137/080730238.

[37] S. Haker, L. Zhu, A. Tannenbaum, and S. Angenent, *Optimal mass transport for registration and warping*, Int. J. Comput. Vis., 60 (2004), pp. 225–240.

[38] J. S. Hesthaven, G. Rozza, and B. Stamm, *Certified Reduced Basis Methods for Parametrized Partial Differential Equations*, SpringerBriefs Math., Springer, Cham; BCAM Basque Center for Applied Mathematics, Bilbao, Spain, 2016, https://doi.org/10.1007/978-3-319-22470-1.

[39] D. Huynh, G. Rozza, S. Sen, and A. T. Patera, *A successive constraint linear optimization method for lower bounds of parametric coercivity and inf-sup stability constants*, C. R. Math. Acad. Sci. Paris 345 (2007), pp. 473–478.

[40] D. B. P. Huynh, D. J. Knezevic, Y. Chen, J. S. Hesthaven, and A. T. Patera, *A natural-norm successive constraint method for inf-sup lower bounds*, Comput. Methods Appl. Mech. Engrg., 199 (2010), pp. 1963–1975.

[41] L. V. Kantorovich, *On a problem of Monge*, J. Math. Sci. (N.Y.), 133 (2006), 1383.

[42] Y. N. Kiseliov, *Algorithms of projection of a point onto an ellipsoid*, Lith. Math. J., 34 (1994), pp. 141–159.

[43] S. Kolouri and G. K. Rohde, *Transport-based single frame super resolution of very low resolution face images*, in Proceedings of the IEEE Conference on Computer Vision and Pattern Recognition, 2015, pp. 4876–4884.

[44] S. Kolouri, Y. Zou, and G. K. Rohde, *Sliced Wasserstein kernels for probability distributions*, in Proceedings of the IEEE Conference on Computer Vision and Pattern Recognition, 2016, pp. 5258–5267.

[45] R. Lai and H. Zhao, *Multi-scale Non-rigid Point Cloud Registration Using Robust Sliced-Wasserstein Distance via Laplace-Beltrami Eigenmap*, preprint, https://arxiv.org/abs/

1406.3758, 2014.

[46] K. Lee and K. T. Carlberg, *Model reduction of dynamical systems on nonlinear manifolds using deep convolutional autoencoders*, J. Comput. Phys., 404 (2020), 108973.

[47] T. L. Lewis, *Finite Difference and Discontinuous Galerkin Finite Element Methods for Fully Nonlinear Second Order Partial Differential Equations*, Ph.D. thesis, University of Tennessee, Knoxville, TN, 2013.

[48] P. Li, Q. Wang, and L. Zhang, *A novel earth mover's distance methodology for image matching with Gaussian mixture models*, in Proceedings of the IEEE International Conference on Computer Vision, 2013, pp. 1689–1696.

[49] G. Monge, *Mémoire sur la théorie des déblais et des remblais*, De l'Imprimerie Royale, Paris, 1781.

[50] G. Montavon, K. R. Müller, and M. Cuturi, *Wasserstein Training of Boltzmann Machines*, preprint, https://arxiv.org/abs/1507.01972, 2015.

[51] J. A. Ozolek, A. B. Tosun, W. Wang, C. Chen, S. Kolouri, S. Basu, H. Huang, and G. K. Rohde, *Accurate diagnosis of thyroid follicular lesions from nuclear morphology using supervised learning*, Med. Image Anal., 18 (2014), pp. 772–780.

[52] A. V. Pogorelev, *The Dirichlet problem for the multidimensional analogue of the Monge-Ampere equation*, Dokl. Akad. Nauk SSSR, 12 (1971), pp. 790–793.

[53] A. Quarteroni, A. Manzoni, and F. Negri, *Reduced basis methods for partial differential equations: An introduction*, Unitext. 92, Springer, Cham, 2016.

[54] R. Rockafellar, *Characterization of the subdifferentials of convex functions*, Pacific J. Math., 17 (1966), pp. 497–510.

[55] F. Romor, G. Stabile, and G. Rozza, *Non-linear Manifold ROM with Convolutional Autoencoders and Reduced Over-collocation Method*, preprint, https://arxiv.org/abs/2203.00360, 2022.

[56] Y. Rubner, C. Tomasi, and L. J. Guibas, *The earth mover's distance as a metric for image retrieval*, Int. J. Comput. Vis., 40 (2000), pp. 99–121.

[57] M. Sulman, J. F. Williams, and R. D. Russell, *Optimal mass transport for higher dimensional adaptive grid generation*, J. Comput. Phys., 230 (2011), pp. 3302–3330.

[58] N. Trudinger and X. J. Wang, *On the second boundary value problem for Monge-Ampere type equations and optimal transportation*, Ann. Sc. Norm. Super. Pisa Cl. Sci. (5), 8 (2009), pp. 143–174.

[59] J. Urbas, *On the second boundary value problem for equations of Monge-Ampère type*, J. Reine Angew. Math., 487 (1997), pp. 115–124.

[60] J. I. E. Urbas, *The generalized Dirichlet problem for equations of Monge-Ampère type*, Ann. Inst. H. Poincaré C Anal. Non Linéaire, 3 (1986), pp. 209–228.